Comparison of Wind-Tunnel and Flight Unsteady Pressure Stochastic Characteristics for the Space Launch System Artemis I Flight

Patrick S. Heaney[*], David J. Piatak[†], Oleg Goushcha[*], James M. Ramey[*], Francesco Soranna[*], and Martin K. Sekula[‡]
NASA Langley Research Center, Hampton, VA, 23681

Over the course of more than ten years, numerous wind tunnel tests have been conducted to acquire data for characterizing the unsteady pressure environments expected to act on the Space Launch System Block 1 crew launch vehicle during ascent. These wind tunnel tests of highly-instrumented rigid models are the current standard for the estimation of unsteady environments. Following the successful launch of the Artemis I mission, the extensive flight data acquired can be analyzed to evaluate the accuracy of unsteady pressure environments predicted in subscale wind tunnel testing in comparison to the flight test data. In this paper, analyses focusing on data from several Space Launch System wind-tunnel tests and the Artemis I flight test are presented, including assessments of test-to-test, tunnel-to-tunnel, and tunnel-to-flight stochastic characteristics and preflight modeling validity based on wind tunnel testing. In general, the fluctuating pressure environments measured during several preflight subscale wind-tunnel tests compare favorably and provide relatively accurate estimates of the environments measured during flight. Discrepancies in fluctuating magnitudes, spatial extent of regions of unsteadiness, and narrowband frequency peaks are noted in the multibody region aft of the solid rocket booster forward attachment to the core stage.

Note to the Reader

The Space Launch System, including its predicted performance and certain other features and characteristics, have been defined by the U.S. Government to be Controlled Unclassified Information (CUI). Information deemed to be CUI requires special protection and may not be disclosed to an international audience. To comply with CUI restrictions, details such as absolute values have been removed from some plots and figures in this paper. It is the opinion of the authors that despite these alterations, there is no loss of meaningful technical content. Analytical methodologies and capabilities are discussed, significant and interesting technical results are still present, and meaningful conclusions are presented.

Acronyms

ARC = Ames Research Center
B1 = Block 1
B1B = Block 1B
BET = best estimated trajectory
BFF = buffet forcing function
BSTR = booster
CCJ = cone cylinder junction
CWT = continuous wavelet transform
DFI = developmental flight instrumentation
FAH = forward attachment hardware
FDA = flight data analysis
FTO = flight test objectives
LOX = liquid oxygen
LSRB = left solid rocket booster
LVSA = launch vehicle stage adapter
LaRC = Langley Research Center
MPCV = multi-purpose crew vehicle
PSD = power spectral density
PT = pressure transducer
RBM = rigid buffet model
RSRB = right solid rocket booster
SLS = Space Launch System
SM = service module
SRB = solid rocket booster

---

[*] Research Aerospace Engineer, Aeroelasticity Branch, MS 340, AIAA Member.
[†] Assistant Branch Head, Aeroelasticity Branch, MS 340, AIAA Senior Member.
[‡] Senior Research Aerospace Engineer, Aeroelasticity Branch, MS 340.

ICPS = interim cryogenic propulsion stage
IE = Induced Environments
KDE = kernel density estimate
LAS = launch abort system
LDI = Loads, Dynamics, and Integration
LH2 = liquid hydrogen
SWT = Supersonic Wind Tunnel
TDT = Transonic Dynamics Tunnel
TWT = Transonic Wind Tunnel
UPWT = Unitary Plan Wind Tunnel
WT = wind tunnel

Nomenclature

C_p = pressure coefficient
C_p' = fluctuating pressure coefficient
D = reference diameter
f = frequency
M_∞ = freestream Mach number
ms = model scale
p = pressure
q_∞ = freestream dynamic pressure
Re_D = Reynolds number based on core diameter D
rms = root mean square
t = time
U_∞ = freestream velocity
x,y,z = longitudinal, lateral, and vertical body axes
α = angle of attack
β = sideslip angle
θ = body coordinate system clocking angle
Φ = power spectral density

I. Introduction

Launch vehicle buffet environments arise from the unsteady external pressure field during atmospheric ascent that can force local and global vehicle structural responses. Contributing flow features can include boundary layer separation, shock oscillations, flow reattachment, vortex shedding, wake impingement, and multibody effects, notionally depicted in Fig. 1 along with a representative Space Launch System (SLS) Block 1 crew global vehicle bending mode that can respond to these forces. Each of these flow environments can generate significant external aerodynamic forces and the resulting buffet responses, structural buffet loads, and impacts on avionics and secondary structures must be shown to be within the capabilities and margins of safety of the launch vehicle when considered with all other load environments [1, 2]. These buffet environments must be considered in the design cycles of a combined launch vehicle and payload using suitable buffet forcing functions (BFFs) that are typically obtained via highly instrumented wind-tunnel (WT) models tested in transonic and supersonic test facilities. The technique of combining buffet forcing function environments with other load environments such as aeroacoustic, ignition overpressure, steady aerodynamic line loads, and more is known as coupled loads analysis and involves application of these environment loads to a vehicle finite element model that represents the vehicle structure bounded within key flight regimes based on trajectory freestream Mach number (M_∞). The BFFs and resulting vehicle responses and loads are highly dependent on vehicle shape, trajectory and modal properties of the vehicle. Typically, buffet environments are most severe in the transonic regime and can be the largest contributor to vehicle responses and loads during that portion of ascent [3–5].

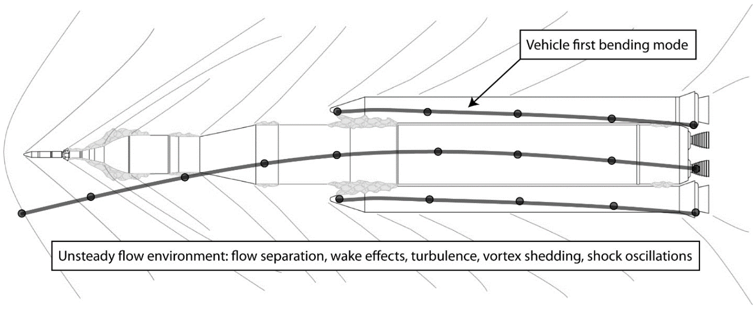

Fig. 1 Notional unsteady flow environment and structural deflection for SLS Block 1 crew configuration.

The BFFs used in design of the SLS Block 1 crew vehicle were obtained from a WT test campaign in 2014 at the NASA Langley Research Center (LaRC) Transonic Dynamics Tunnel (TDT) using a highly instrumented 3%-scale rigid buffet model (RBM) representing the SLS Block 1 crew configuration (SLS-10005). This configuration represents the Artemis I launch configuration at that stage of development and was a modification of the WT model tested in 2012, which initially revealed high buffet environments associated with the booster forward attachment hardware and gap region between booster and core stage. The second WT test in 2014 was part of a buffet mitigation task team that sought to understand this environment and its impact on vehicle loads. Both tests and proposed buffet mitigation options are discussed in detail in Refs. [6–9] and the source of these WT-observed buffet environments and comparison to flight measurements will be the subject of further discussion in this paper.

Early in the SLS developmental flight instrumentation (DFI) design effort, one key focus of the Induced Environments (IE) team was on assuring that the program would capture key unsteady aerodynamic environments for the purpose of post-flight loads reconstruction. Even for a first flight of a new crewed vehicle, Artemis I carried an unprecedented 2,270 DFI sensors to support flight test objectives to observe vehicle performance across numerous design disciplines and vehicle elements [10]. Buffet and its parent IE team supported the structures and environments flight test objectives (FTO) and the Loads Dynamics and Integration (LDI) team, with the buffet FTO intending to anchor and validate the underlying methods and tools represented by the BFF database using the Artemis I flight data measurements. To achieve this objective, 183 unsteady aerodynamic DFI sensors were designated on the Artemis I vehicle for buffet environments by the IE team with the majority of these external sensors having identical analogs to those on the RBM used as part of BFF development program.

This paper will provide a review of the wind tunnel test campaigns used to characterize the predicted unsteady pressure environments during the ascent of Artemis I. These data from WT tests were used to develop the preflight buffet environments implemented in vehicle design analysis cycles. Assessments of the repeatability of important metrics associated with several WT tests will be discussed, and comparisons of fluctuating pressure environments from the Artemis I DFI data will be made with those from WT tests of several SLS launch vehicle configurations. Data presented will include root mean squared and spectral density comparisons of fluctuating pressure coefficient to assess the validity of the preflight buffet environments.

II. Background

A. Wind Tunnel Tests

Numerous wind tunnel tests have been conducted during the SLS program characterizing blocks and revisions of the crew and cargo launch vehicle configurations at both the NASA LaRC TDT and the NASA Ames Research Center (ARC) Unitary Plan Wind Tunnel (UPWT) 11-Foot Transonic Wind Tunnel (11-Ft TWT) and 9- by 7-Foot Supersonic Wind Tunnel (9x7 SWT). Table 1 presents a summary of tests that have been related to buffet and aeroacoustic environments and are discussed in this paper. Photographs of the SLS RBMs for which data are discussed in this paper are presented in Fig. 2, which includes models tested during: (1) LaRC TDT Test 645, (2) ARC UPWT Ascent Unsteady Aerodynamics Test (AUAT), (3) ARC UPWT Ascent Transient Aerodynamics Test (ATAT), and (4) LaRC TDT Test 668. Wind tunnel tests at the ARC UPWT were conducted in air, while R134a (heavy gas) test medium was used for the majority of the data acquired at the LaRC TDT. Limited data are also acquired in air at TDT during these tests for Reynolds number and test medium sensitivity studies.

The RBM tested during the LaRC TDT Test 645 served as the final buffet test configuration of the Block 1 crew configuration that would support the Artemis I mission and employed a high sensor density to observe buffet environments more accurately downstream of the booster-to-core forward attachment. Since data acquired during this test were used in the development of the BFF database for Artemis I, other tunnel and flight data will primarily be compared against this test. The RBM core and boosters were based on the SLS-10003 early look design with updated protuberances to reflect the SLS-10005 configuration. The RBM is shown in Fig. 2a mounted on the sting and roll coupler in the TDT test section.

B. Artemis I Flight

The sensor locations for external aerodynamic environments for the SLS Block 1 crew configuration flown as part of Artemis I were largely based on sensor locations from the WT tests described above. Of the 2,270 DFI sensors flown on Artemis I, there were 289 external aerodynamic sensors intended to be used as part of each launch vehicle environment flight data analysis (FDA) task in support of SLS program FTOs. Of these 289 aerodynamic sensors, 183 DFI sensors were dedicated to observing the buffet environment and had matching WT sensor data for comparison

Table 1 **Summary of SLS buffet and aeroacoustic wind tunnel tests analyzed in this study.**

Test	NASA facility	Year	SLS configuration	Model scale
Test 645	LaRC TDT	2013-2014	SLS-10005 Block 1 crew FAH buffet mitigation options	3%
Ascent Unsteady Aerodynamics Test (AUAT) T11-0344/T97-0345	ARC UPWT 11-Ft TWT / 9x7 SWT	2017-2018	SLS-27005 Block 1B cargo SLS-28005 Block 1B crew	2.5% (full-stack) 4% (forebody)
Ascent Transient Aerodynamics Test (ATAT) T11-0377/T97-0376	ARC UPWT 11-Ft TWT / 9x7 SWT	2019	SLS-10506 Block 1 cargo SLS-27005 Block 1B cargo	2.5% (full-stack)
Test 668	LaRC TDT	2022	SLS-28006 Block 1B crew SLS-27005 Block 1B cargo	3%

at nearly identical locations. Some buffet sensors were shared by other environments, including ascent aeroacoustics and ignition overpressure, and thus had sample rates set according to the highest frequency of interest for all shared environments. Figure 3 summarizes the stations corresponding to buffet sensor rings on the RBM as tested during the TDT Test 645 in comparison to those corresponding to the DFI sensor arrangement for Artemis I. While there were aerodynamic DFI instrumenting the right solid rocket booster (RSRB), no rings of unsteady pressure sensors were placed on that body for buffet environment data reduction and comparison to the BFF database, so only the core and left SRB (LSRB) stations are shown.

During prelaunch vehicle tanking activities, including hot fires, launch attempts, and tanking test, sensors in several regions of the vehicle on the core stage experienced port icing that partially or fully blocked the sensor orifice. These sensors were mainly located on the cryogenic tanks (liquid oxygen (LOX) and liquid hydrogen (LH2) tanks), leading to severely degraded or unusable data for many sensors in these regions. At station 25, for example, all six azimuthally spaced sensors experienced icing during the Artemis I launch. The ice blockage at one of these sensors, located at clocking angle θ = 90°, was liberated during ascent and led to valuable data being acquired during the remainder of flight for this critical region of the vehicle.

III. Methodology

In this section, brief descriptions of the methodologies used to analyze flight and tunnel data in this paper are provided (following the same methods described in Ref. [11]). Analyses focus on comparisons at the core stage stations shown in Fig. 4, which are representative of several unsteady pressure environments present on the SLS launch vehicle and are stations where pressure transducers (PTs) are closely located for both the Test 645 RBM and the Artemis I flight vehicle:

1) **station 4**: launch abort system (LAS), in the wake of the LAS nozzles
2) **station 8**: service module (SM), aft of the multi-purpose crew vehicle (MPCV) to SM shoulder
3) **station 13**: launch vehicle stage adapter (LVSA), aft of interim cryogenic propulsion stage (ICPS) to LVSA compression corner and recirculation zone
4) **station 16**: forward skirt, aft of the LVSA to forward skirt cone cylinder junction (CCJ)
5) **station 25**: LH2 tank, in the multibody region downstream of the booster forward attachment hardware
6) **station 33**: engine section, in the multibody region downstream of the booster aft attachment hardware

Limited results will also be presented for PTs located at several other stations. Throughout the paper, PT locations will be referenced by the longitudinal x-station number from TDT Test 645 (shown in Fig. 3) and the clocking angle, θ, defined for the core and SRBs according to the convention shown in Fig. 5.

(a) Block 1 crew 3%-scale RBM tested during the LaRC TDT Test 645.

(b) Block 1B cargo 2.5%-scale RBM (tangent-ogive payload fairing) tested during the ARC UPWT AUAT.

(c) Block 1B crew 3%-scale RBM tested during the LaRC TDT Test 668.

(d) Block 1B crew 4%-scale RBM tested during the ARC UPWT AUAT.

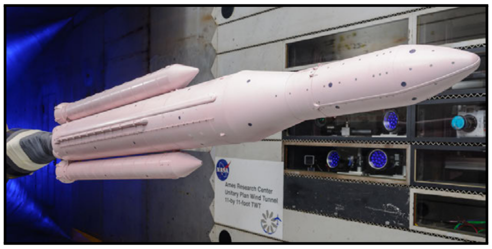

(e) Block 1 cargo 2.5%-scale RBM tested during the ARC UPWT ATAT. Model surface painted with unsteady pressure sensitive paint.

Fig. 2 SLS launch vehicle RBMs analyzed in this study [Source: NASA].

A. Flight Data

The first challenge in analyzing unsteady pressure data using absolute pressure data acquired during the flight test is the estimation and removal of the constantly varying trend due to changing flight conditions. As an example of the flight data processing, Fig. 6a presents measured pressures for a PT located at analysis station 25 and a clocking angle $\theta = 90°$. In this figure, the black curve represents the estimated steady component of the pressure time history using a moving mean calculated with a duration of 0.5 s. This sensor, located on the LH2 cryogenic tank, was iced over during the first part of flight, and therefore, measured no fluctuating pressures. After the ice was liberated, the sensor signal provided valuable data in the most critical region of the vehicle downstream of the booster forward attachment hardware.

Figure 6b presents wideband and bandpass filtered time histories for the detrended pressure coefficient after removing the steady trend, where a bandpass filter between 0.5 to 100 Hz full scale has been used to focus on the bandwidth generally considered important for buffet excitation of global vehicle flexible dynamics. For this fluctuating signal example, most of the energy is within that bandwidth, so the wideband and bandpass filtered data are overwhelmingly the same. Figure 6c presents a summary of the moving window root mean square (rms) of the detrended pressure coefficient, $C'_{p,\mathrm{rms}}$, where the window for the moving rms has a duration of 0.5 s.

In comparison to WT testing, when relatively long records are acquired to better characterize the stationary stochastic processes with converged estimates of the underlying distribution, during flight the freestream aerodynamic conditions and vehicle attitude are constantly varying. The nonstationary nature of the fluctuating pressure stochastic processes during accelerating flight thus results in much shorter duration M_∞ windows relative to tunnel data records over which

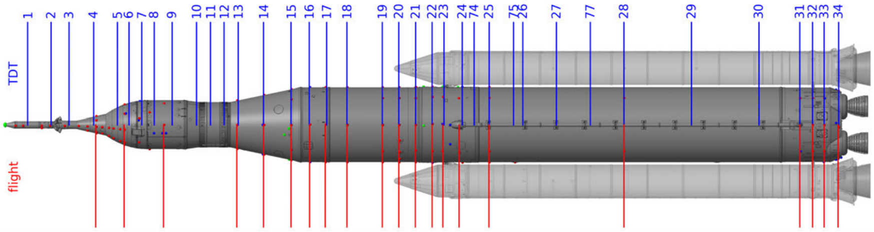

(a) Core.

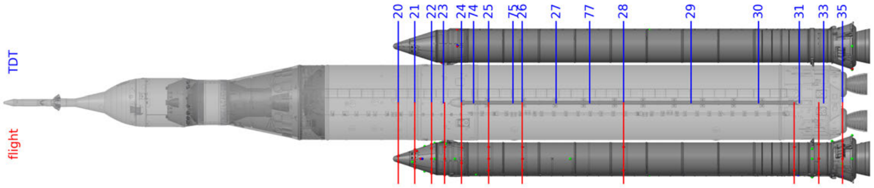

(b) LSRB.

Fig. 3 Artemis I DFI buffet stations in comparison to Test 645.

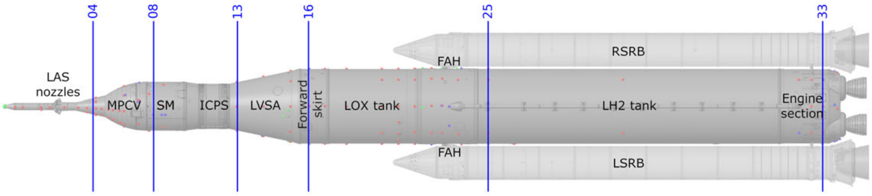

Fig. 4 Analysis stations. Vehicle components referenced in this paper are also annotated.

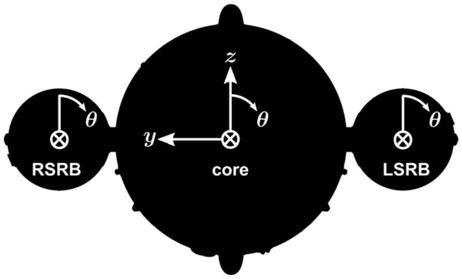

Fig. 5 Body coordinate system convention for clocking angle, θ. View in the aft facing, $+x$, direction.

the flow physics may be approximated as quasistationary. In addition, there is no expectation that estimated statistics of the underlying distribution are converged. For these reasons, the flight data are processed using moving windows of relatively short duration, and as will be shown below, the long record tunnel data are processed using windows of the same scaled duration to generate prediction distributions of quantities of interest ($C'_{p,\mathrm{rms}}$ and C'_p spectra, for example) to compare with flight data.

B. Wind Tunnel Data

Several WT tests have been conducted throughout the SLS program to characterize the unsteady pressure environments predicted to act on the vehicle during ascent. The test matrices for these tests have covered a wide variety of aerodynamic conditions, such as M_∞, freestream dynamic pressure (q_∞), freestream velocity (U_∞), and Reynolds number (Re), as well as vehicle orientations defined by angles of attack α and sideslip β. In Section IV.A, repeat point data (where the aerodynamic conditions and vehicle orientations are within small bounds of each other) from Test 645 are compared to assess variability present in the unsteady data acquired within a single test. In Section IV.B, similar comparisons

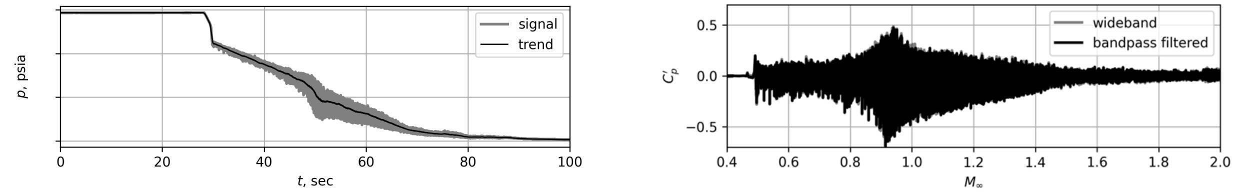

(a) Signal time history and trend based on 0.5 s moving mean windows shown in black.

(b) Fluctuating pressure coefficient.

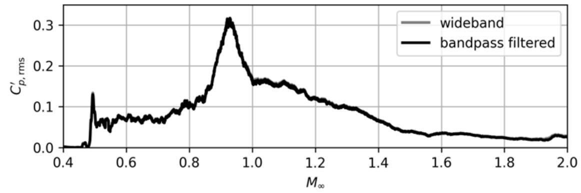

(c) $C'_{p,\mathrm{rms}}$ based on moving window rms.

Fig. 6 Artemis I flight data example processing for PT at station 25, $\theta = 90°$.

are presented across several WT tests to assess the variability present between tests and between the two test facilities. Results in both of these sections utilize data from the WT tests acquired at $\alpha = \beta = 0°$ vehicle orientations. While attitude variations can have an important effect on the unsteady pressure field, thus limiting the scope of applicability for the results presented outside the small α_{total} domain, it is deemed more important to have as many repeat test points as possible for the assessment of point-to-point and test-to-test repeatability. Since the most repeat points during these WT test are acquired at $\alpha = \beta = 0°$, these points are used for the repeatability assessment.

Later, in Section IV.C, where WT data are compared to flight, data from both the $\alpha = \beta = 0°$ repeats and from points where the vehicle attitude best matches the Artemis I best estimated trajectory (BET) are presented. Since α_{total} is relatively small for the Artemis I BET, it is deemed a reasonable compromise to present some WT comparisons using the matched attitude condition and others using the many repeats available at $\alpha = \beta = 0°$. For each M_∞ acquired during Test 645, the matched attitude WT test point minimizes the sum of squared differences for the corresponding flight α and β.

Since data from tests of several different WT models fabricated at several geometric scales are analyzed in this paper (model scales summarized in Table 1), all results are scaled to the Artemis I full-scale vehicle and BET using rigid buffet scaling laws. In this paper, unsteady pressures have been normalized as C'_p to compare tunnel and flight conditions at different dynamic pressures, and time and frequencies have been scaled based on a reduced frequency. The relationships used for scaling are presented in Table 2. Although many WT parameters can be matched or scaled, the Reynolds number, Re_D, based on the core stage diameter is an order of magnitude lower for the WT test points than for the flight. Although trip strips were applied to the models during all SLS WT tests to cause the boundary layer to transition at appropriate model locations on the core stage and boosters, given the importance of Reynolds number in simulating the unsteady flow field these differences are potentially important in interpreting comparisons between tunnel and flight data [12].

Table 2 Rigid buffet scaling laws based on the reference diameter, D, dynamic pressure, q_∞, and velocity, U_∞.

Quantity to be scaled	Full-scale (fs) to model-scale (ms) relation
Pressure, p	$p_{\mathrm{fs}} = p_{\mathrm{ms}} \frac{q_{\infty,\mathrm{fs}}}{q_{\infty,\mathrm{ms}}}$
Time, t	$t_{\mathrm{fs}} = t_{\mathrm{ms}} \frac{D_{\mathrm{fs}}}{D_{\mathrm{ms}}} \frac{U_{\infty,\mathrm{ms}}}{U_{\infty,\mathrm{fs}}}$
Frequency, f	$f_{\mathrm{fs}} = f_{\mathrm{ms}} \frac{D_{\mathrm{ms}}}{D_{\mathrm{fs}}} \frac{U_{\infty,\mathrm{fs}}}{U_{\infty,\mathrm{ms}}}$
Pressure PSD, Φ^p (psi^2/Hz)	$\Phi^p_{\mathrm{fs}} = \Phi^p_{\mathrm{ms}} \left(\frac{q_{\infty,\mathrm{fs}}}{q_{\infty,\mathrm{ms}}}\right)^2 \frac{D_{\mathrm{fs}}}{D_{\mathrm{ms}}} \frac{U_{\infty,\mathrm{ms}}}{U_{\infty,\mathrm{fs}}}$

An example of the steps used to process the tunnel data is shown in Fig. 7, where the full duration time history acquired in the WT during Test 645 and estimated trend are shown in Fig. 7a for a PT located at station 25. The WT data are processed in a similar way to the flight data, using time windows of scaled duration corresponding to equivalent flight durations. By analyzing the WT data in a manner similar to the flight data, each WT test point contains many realizations of scaled-to-flight time windows, and corresponding prediction distributions based on the statistics for the ensemble of these realizations can be compared to flight data. As such, although removing the signal mean or low order polynomial fit is sufficient for detrending WT pressure time histories, for consistency in processing with the flight data the WT trend is determined using a moving mean calculated with a full scale duration of 0.5 s. For this example, the 0.5 s full scale window scales to a model scale duration of approximately 0.028 s (450 samples for data acquired at 16 kHz during TDT Test 645). The wideband and bandpass filtered time histories of C_p' are shown in Fig. 7b. For this example at $M_\infty = 0.95$ for the 3%-scale RBM, the 0.5 to 100 Hz full-scale bandpass filter bandwidth scales to a model scale bandwidth of approximately 8.9 to 1,779 Hz.

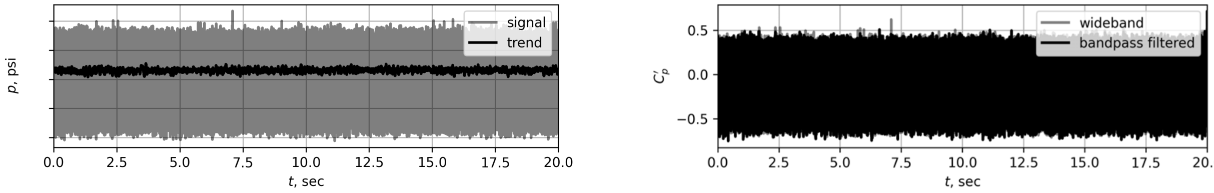

(a) Signal time history. Moving mean trend based on scaled 0.5 s full-scale windows shown in black.

(b) Fluctuating pressure coefficient.

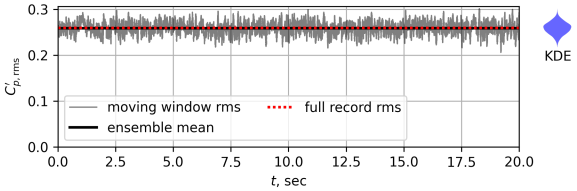

(c) $C_{p,\text{rms}}'$ based on moving window rms, corresponding ensemble mean, and full record rms. KDE of the probability distribution for $C_{p,\text{rms}}'$ realizations plotted to the right.

Fig. 7 WT data example processing for PT at station 25, $\theta = 90°$, at $M_\infty = 0.95$.

The moving window rms of the filtered C_p' for realizations of scaled duration corresponding to the matching flight window is shown in Fig. 7c. The ensemble mean of the moving window rms values and rms of the full time record, which compare well, are plotted for reference. To give an indication of the variability of the estimated WT $C_{p,\text{rms}}'$, the kernel density estimate (KDE) of the $C_{p,\text{rms}}'$ probability distribution is shown as a violin plot to the right in this figure. Assessments of the spread of the KDE will be discussed in the results section to provide context for comparisons to flight data and indicators of particular regions on the vehicle and tunnel conditions at which the $C_{p,\text{rms}}'$ realizations have high variability.

IV. Results

In this section, comparisons of unsteady pressure environments using $C_{p,\text{rms}}'$ and the power spectral density (PSD) of C_p' are presented. First, results related to point-to-point repeatability for Test 645 are discussed, and then corresponding results for several other WT tests are compared. Assessments of the WT environments are then made in comparison to data acquired during the Artemis I flight test.

A. Comparison of Fluctuating Pressures, WT Point to Point

Results presented in this section compare the unsteady pressure environments measured for repeat points at $\alpha = \beta = 0°$ during Test 645. One measure of point-to-point repeatability is how much $C_{p,\text{rms}}'$ varies over the course of the test for repeat points. In Fig. 8, data acquired for 22 repeat points at $\alpha = \beta = 0°$ and $M_\infty = 0.95$ are presented for PTs at the representative analysis stations. For each point, a scaled moving window corresponding to 0.5 s full-scale duration is used to compute the ensemble of $C_{p,\text{rms}}'$, and the resulting (1) ensemble mean and (2) upper and lower bounds that represent the 2.5- to 97.5-percentile range (95% of the $C'_{p,\mathrm{rms}}$ ensemble) are plotted.

In addition, data for all repeats are concatenated for each comparison PT and the mean and corresponding 95% bounds for all records combined are plotted for reference. Generally, sensor $C'_{p,\mathrm{rms}}$ point-to-point repeatability during Test 645 is relatively consistent, with the ensemble means generally varying between points less than the variability for flight-representative sample windows within a single point. Throughout the test, the 95% bounds are also relatively consistent.

A significant source of variability in the ensemble mean $C'_{p,\mathrm{rms}}$ between points appears to be related to model roll angle within the test section. In Fig. 9, the ensemble mean $C'_{p,\mathrm{rms}}$ for the 22 repeat points is plotted against the model roll angle. Trends in $C'_{p,\mathrm{rms}}$ are present for all PTs presented, with the most significant differences appearing for stations 16 and 25, where small changes in vehicle attitude would be expected to yield larger differences in fluctuating pressure environments due to the nature of the flowfield in those locations.

As can be seen in Figs. 8 and 9, fluctuating pressure magnitudes for the analysis stations presented are highest downstream of the booster-to-core forward attachment hardware (FAH). A closeup view of the FAH on the TDT RBM is shown in Fig. 10. Multibody configurations like the SLS can result in challenging buffet environments due to the interaction of flow phenomenon in the vicinity of the SRB and core stage attachment regions. At transonic conditions, the shock that forms at the expansion corner of the SRB nose cone-cylinder junction just upstream of the booster forward attachment protuberance is easily perturbed by the unsteady environment (vortex shedding wake) behind this protuberance, and a strong interaction between the expansion shock and shed wake can develop with distinct narrowband frequency peaks corresponding to unsteady pressure modes associated with the FAH wake [13].

This environment has been shown to be quite sensitive to the forward attachment protuberance geometry and vehicle attitude. To illustrate the sensitivity to vehicle attitude, the peak buffet environment $C'_{p,\mathrm{rms}}$ trend with respect to a β sweep between ±6° at $M_\infty = 0.95$ and $\alpha = 0°$ is shown in Fig. 11a. Data for PTs on the core at $\theta = 90°$ in the LSRB gap region and at $\theta = 270°$ in the RSRB gap region downstream of the booster FAH are presented. Note that peak $C'_{p,\mathrm{rms}}$ occurs on the windward side of the vehicle ($\theta = 90°$ for $\beta = -6°$ and $\theta = 270°$ for $\beta = +6°$) and increases with sideslip at station 25 and at stations downstream. The corresponding sensitivity of the buffet environment at $M_\infty = 0.95$ to a sweep in α between ±6° for $\beta = 0°$ is shown in Fig. 11b. Here, as α increases the peak $C'_{p,\mathrm{rms}}$ decreases at station 25, but tends to increase at stations downstream of station 25. Thus, the spatial distribution of the peak environment shifts depending on the vehicle attitude and may not always be fully characterized with spatially discrete PT locations.

At this test condition, a summary of the $C'_{p,\mathrm{rms}}$ repeatability is presented in Fig. 12. In these figures, data for all sensors is plotted to give an overview of the spatial distribution of fluctuating pressure magnitudes, variability, and repeatability. Different markers are used for PTs that are located near the booster (BSTR) plane (x-y plane at $z = 0$ corresponding to the coordinate system in Fig. 5), where the unsteady environments are most elevated in the multibody section of the vehicle, as well as for PTs on the upper and lower surface of the vehicle near the feedlines, which are somewhat elevated due to the local protuberance effects. These notes about the azimuthal variation in $C'_{p,\mathrm{rms}}$ can be observed in Figs. 12a and 12b for the core and LSRB sensors. Figures 12c and 12d present an assessment of how much the test point ensemble means of $C'_{p,\mathrm{rms}}$ vary relative to the mean for all repeats. The largest relative differences based on this metric are located in the same regions where unsteadiness is high, in the vicinity of the CCJ on the forward skirt and downstream of the booster FAH. An interpretation of these figures is that the point-to-point total variation (minimum to maximum) in $C'_{p,\mathrm{rms}}$ reaches a peak of approximately 40% of the mean in some regions of the vehicle, but generally varies approximately 10% to 20% of the mean outside of the peaks and multibody regions.

Similar features are present in Figs. 12e and 12f, where the 95%-bound ranges are plotted in the same manner for the core and LSRB sensors. These indicate the longitudinal regions of the vehicle where the within point variability is relatively high for flight-representative sample windows, similarly pointing to the relative unsteadiness in the booster FAH region. Figures 12g and 12h present an assessment how much that metric of within point variability compares relative to the mean $C'_{p,\mathrm{rms}}$ for all repeats. Here it can be seen that this measure reaches a peak of approximately 80% of the mean in the most unsteady regions of the vehicle and 40% of the mean in the least unsteady regions. Compared to the mean $C'_{p,\mathrm{rms}}$ variability discussed above, this supports the assertion that the mean $C'_{p,\mathrm{rms}}$ repeatability during Test 645 for all PTs varies significantly less than the within point variability for flight-representative sample windows. Thus to characterize the distribution of possible values of $C'_{p,\mathrm{rms}}$ expected to be seen in comparable flight conditions and vehicle attitude, the variability present within a single test point covers more of the possible $C'_{p,\mathrm{rms}}$ distribution than the point-to-point variability.

In addition to the high unsteadiness downstream of the FAH indicated by $C'_{p,\mathrm{rms}}$, the fluctuating pressures in this region of the vehicle are dominated by narrowband spectral peaks associated with the FAH wake vortices [14]. The peak frequencies observed by PTs in the wake downstream of the FAH consists of two distinct tones. The wake behind the

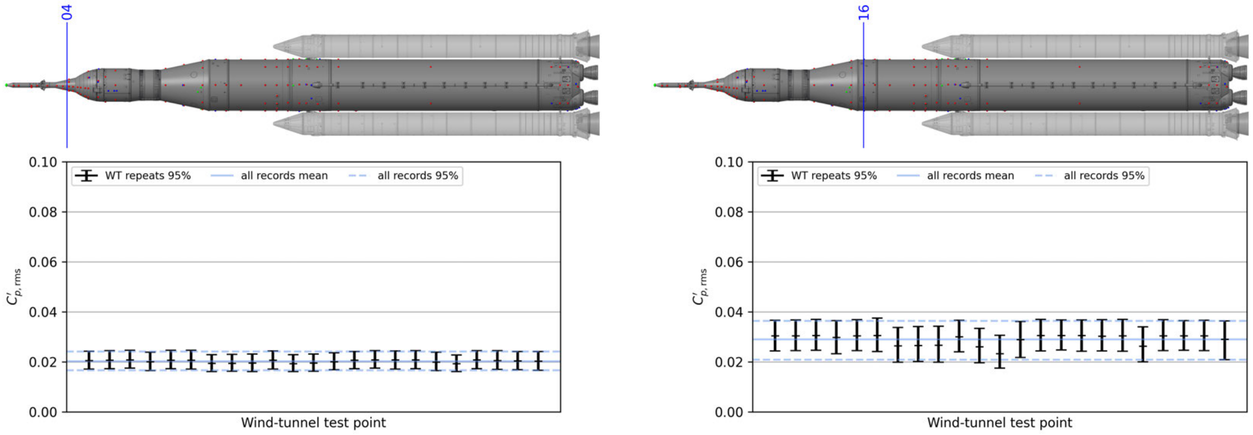

(a) Station 4, $\theta = 90°$**.** **(b) Station 16,** $\theta = 45°$**.**

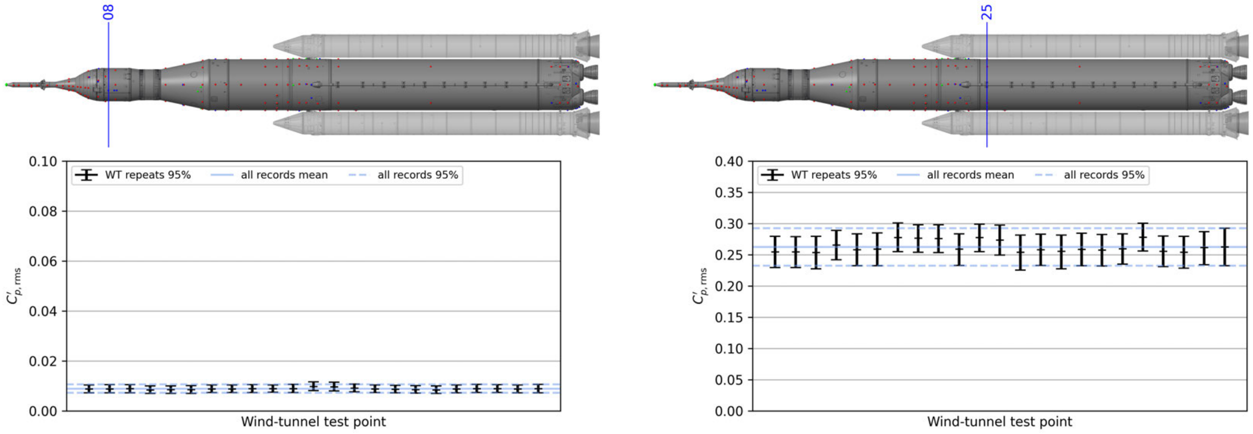

(c) Station 8, $\theta = 90°$**.** **(d) Station 25,** $\theta = 90°$**.**

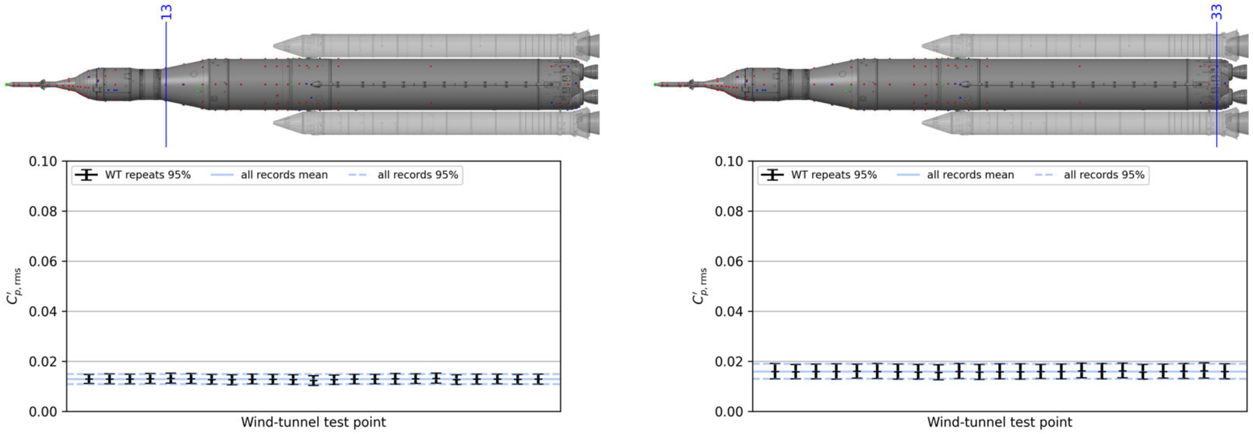

(e) Station 13, $\theta = 90°$**.** **(f) Station 33,** $\theta = 225°$**.**

Fig. 8 $C'_{p,\mathrm{rms}}$ **repeatability during Test 645 for sensors located at the core analysis stations for** $M_\infty = 0.95$ **and** $\alpha = \beta = 0°$**. Data for 22 repeat records are shown and used to compute the** $C'_{p,\mathrm{rms}}$ **means and 95% bounds for all records combined.**

FAH contains alternating shed vortices released from both sides of the FAH and combined, they generate a single, higher frequency tone. There also exists frequency content associated with each individual shed vortex that has a frequency of one-half that of the alternating shed vortices. Depending on the PT location, model attitude, flight condition, one or

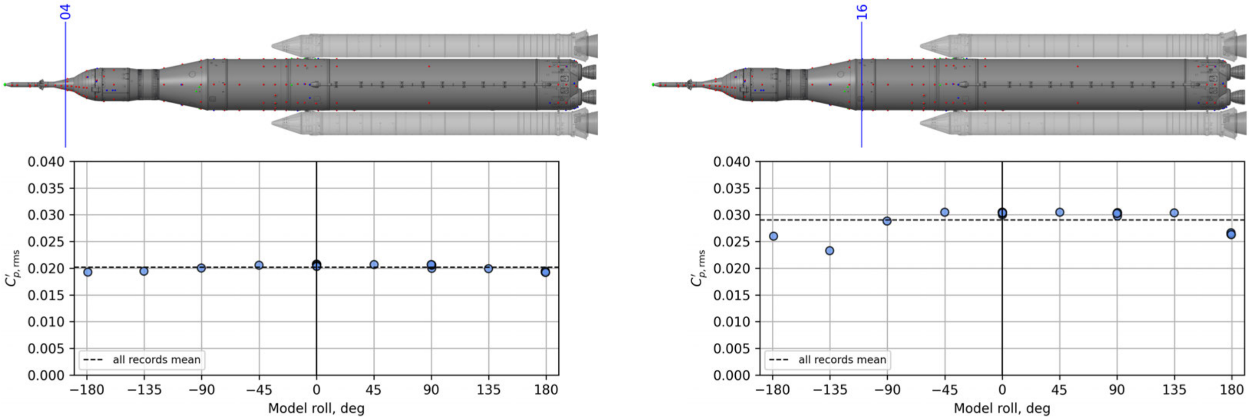

(a) Station 4, θ = 90°. **(b) Station 16,** θ = 45°.

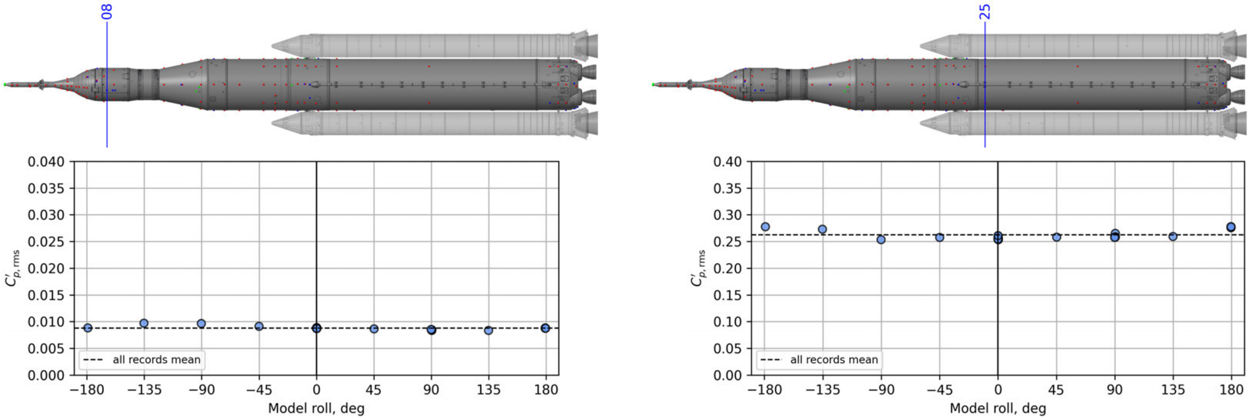

(c) Station 8, θ = 90°. **(d) Station 25,** θ = 90°.

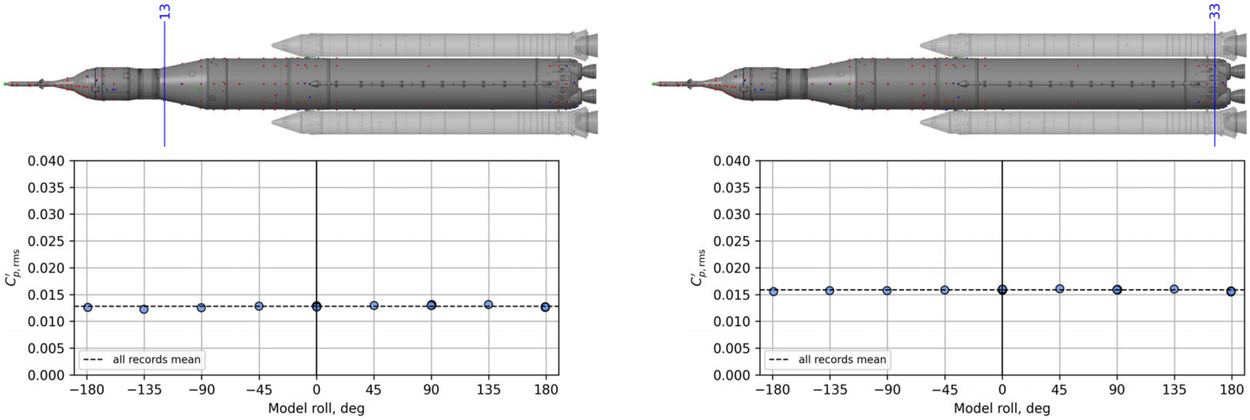

(e) Station 13, θ = 90°. **(f) Station 33,** θ = 225°.

Fig. 9 $C'_{p,\mathrm{rms}}$ **versus model roll angle for sensors located at the core analysis stations for** $M_\infty = 0.95$ **and** $\alpha = \beta = 0°$ **for data acquired during Test 645.**

both peaks may be present and may be relatively stronger or weaker. Another important measure of test repeatability is thus how much those narrowband spectral peaks vary for repeat points. Using two PTs located at station 25 at $\theta = \{90°, 270°\}$ on the booster plane, spectra of C'_p for repeat points are presented in Fig. 13 for several M_∞. Each figure contains blue spectra for a particular M_∞ with $\alpha = \beta = 0°$ overlaid with opacity, and red vertical lines indicating the peak narrowband frequencies identified for each repeat point.

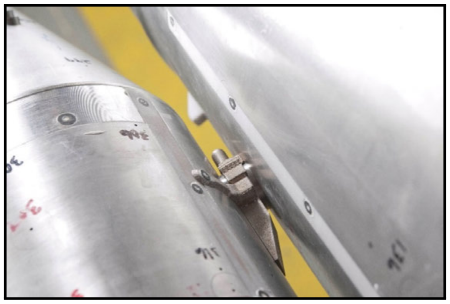

Fig. 10 Test 645 WT model booster-to-core FAH [Source: NASA].

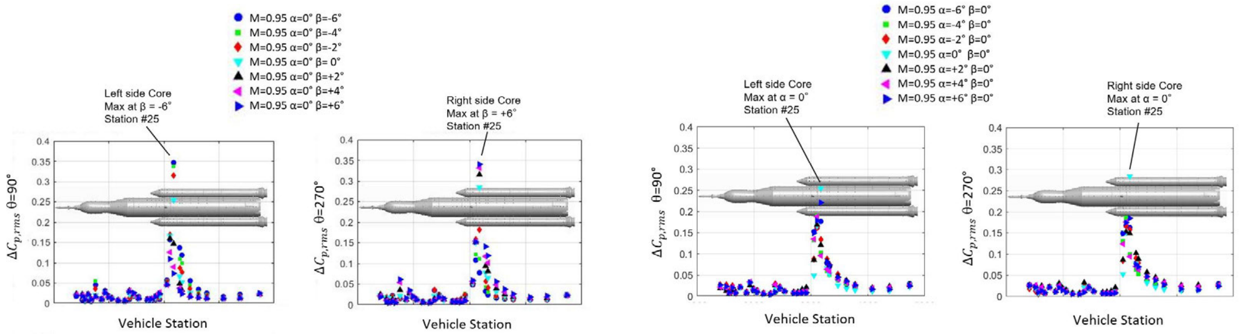

(a) $\alpha = 0°$ **and** β **sweep up to** $\pm 6°$**.**

(b) α **sweep between** $\pm 6°$ **and** $\beta = 0°$**.**

Fig. 11 $C'_{p,\mathrm{rms}}$ **at** $M_\infty = 0.95$ **for PTs on the core at** $\theta = 90°$ **facing the LSRB and at** $\theta = 270°$ **facing the RSRB downstream of the booster FAH.**

As M_∞ increases for the cases shown in Fig. 13, the narrowband peaks broaden and the peak frequencies identified for each repeat point vary more. These data are summarized in Fig. 14, where the more prominent and higher peak is plotted with darker curves and the second lower peak is plotted with lighter curves. For each M_∞ where data are available, the mean peak frequency for all repeats is plotted, as well as the maximum and minimum frequencies identified for each peak. Several observations can be made: (1) the peak frequencies shift with M_∞, with a significant dip centered at $M_\infty \approx 0.92$ occurring between $M_\infty \in [0.85, 0.98]$, (2) there is a relatively consistent offset in peak frequencies identified between the $\theta = 90°$ sensor facing the LSRB and the $\theta = 270°$ sensor facing the RSRB, and (3) the peak frequency variability differs with M_∞, but generally ranges between ±2 Hz of the mean for the more prominent, higher frequency, peak. Figure 14b presents the same data with frequencies normalized by the freestream velocity U_∞, which indicates that the relatively flat curves in the range $M_\infty \in [1.00, 1.18]$ could be adequately modeled using the reduced frequency scaling methodology.

As in the discussion above regarding $C'_{p,\mathrm{rms}}$, a significant source of between point variability in the narrowband spectral peaks downstream of the FAH appears to be related to model roll angle within the test section. Figure 15 illustrates the peak frequencies for repeat points at several M_∞ versus the model roll angle. Trends in identified peak frequencies are observed for all conditions presented: (1) at model roll angle of 0°, the $\theta = 90°$ sensor facing the LSRB has a higher peak than the $\theta = 270°$ sensor facing the RSRB, (2) in general, as the model roll angle moves away from zero toward ±180°, the narrowband peaks decrease for the sensor facing the LSRB and increase for the sensor facing the RSRB. These observations could indicate physically meaningful differences in the peak frequencies due to small model asymmetries, or more likely variations associated with model attitude within the test section or test section flow angularity.

Since the narrowband frequency peaks associated with these unsteady pressure modes are generally dependent upon sensor location, M_∞, and vehicle attitude, small variations in test conditions could lead to observable differences in the identified peaks. The sensitivity of these FAH spectral peaks to changes in β between ±6° at $\alpha = 0°$ for $M_\infty = 0.95$ is shown in Fig. 16a for sensors at clocking angles $\theta = \{90°, 270°\}$ at station 25. The higher frequency mode is quite prominent at these sensor locations, with significant changes in magnitude and frequency with changing β. For the

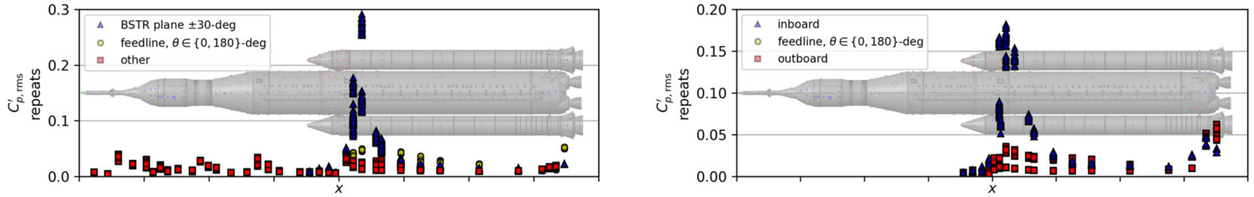

(a) Mean $C'_{p,\mathrm{rms}}$ for core PTs.

(b) Mean $C'_{p,\mathrm{rms}}$ for LSRB PTs.

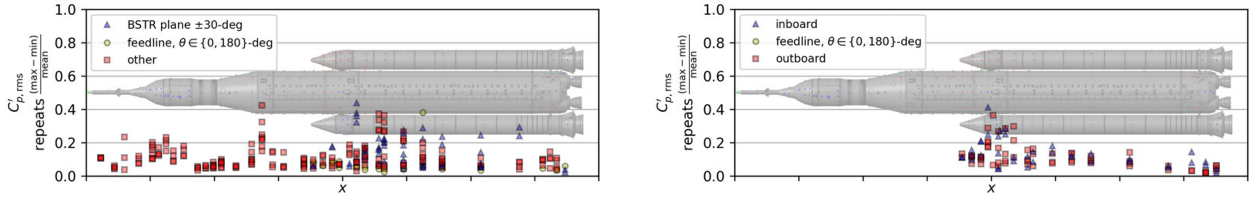

(c) Ratio of maximum to minimum $C'_{p,\mathrm{rms}}$ differences to the mean for core PTs.

(d) Ratio of maximum to minimum $C'_{p,\mathrm{rms}}$ differences to the mean for LSRB PTs.

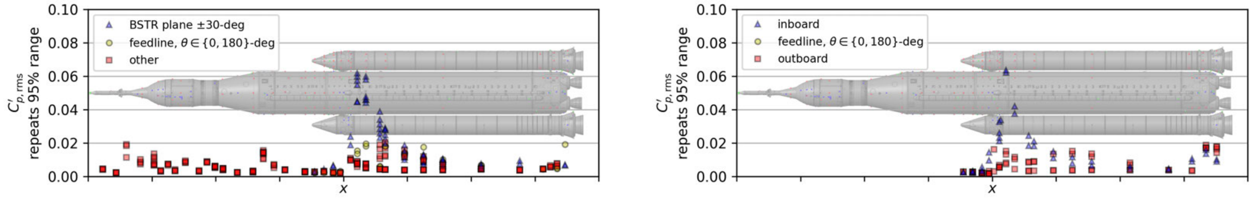

(e) $C'_{p,\mathrm{rms}}$ 95%-bound ranges for core PTs.

(f) $C'_{p,\mathrm{rms}}$ 95%-bound ranges for LSRB PTs.

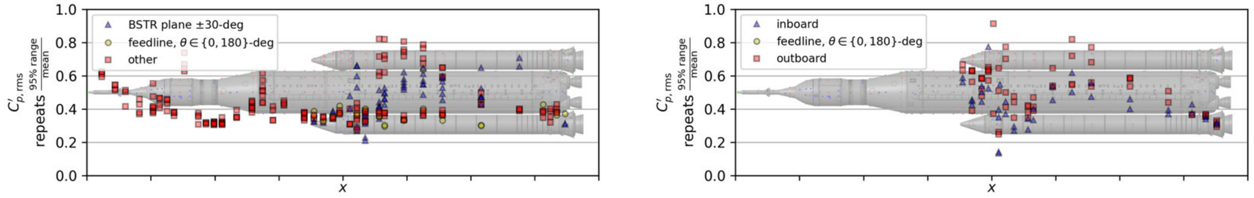

(g) Ratio of $C'_{p,\mathrm{rms}}$ 95%-bound ranges to the mean for core PTs.

(h) Ratio of $C'_{p,\mathrm{rms}}$ 95%-bound ranges to the mean for LSRB PTs.

Fig. 12 $C'_{p,\mathrm{rms}}$ repeatability summary for $M_\infty = 0.95$ and $\alpha = \beta = 0°$ for data acquired during Test 645. Data for 22 repeat points are shown for all PTs versus longitudinal station, x.

sensor on the windward side of the vehicle, the magnitude increase and frequency decrease are both quite large. The change in the frequency peak, for example, is approximately 10 to 12 Hz between $\beta = 0°$ and $|\beta| = 6°$. This sensitivity in peak frequency and magnitude with β can be a challenge for coupled loads analyses and vehicle guidance when other structural components near and downstream of the FAH have structural modes at or near these frequencies.

The sensitivity of the FAH environment frequency and magnitude to α is shown in Fig. 16b. Increasing from $\alpha = 0°$ to $|\alpha| = 2°$, magnitudes for both peaks decrease and the peak frequencies increase. In addition to magnitude and frequency sensitivity to α, the lower frequency mode becomes dominant in the $|\alpha| = 6°$ test data measured at these sensor locations.

The peak transonic buffet environments at $M_\infty = 0.95$ observed in the PTs discussed in Figs. 11 and 16 demonstrate that the FAH environment is highly sensitive to both α and β. Review of sensors azimuthally adjacent to $\theta = 90°$ and $\theta = 270°$ at stations 24 and 25 suggest the FAH environment is highly localized in this region and sensor density plays a key role in adequately observing its spatial distribution. However, the FAH environment and its distinct frequency content can be observed in WT data as far downstream as the engine section of the vehicle. These frequencies have been observed in the WT data to vary between approximately 13 to 29 Hz (lower frequency mode) and 29 to 45 Hz (higher frequency mode). Post-flight data analyses, which will be discussed below, have shown that the FAH environment is also dominant in the external PT signals for the Artemis I flight.

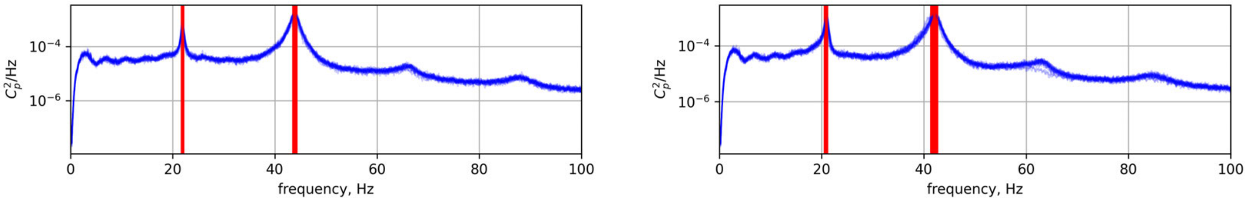

(a) Station 25, θ = 90° **at** M_∞ = 0.80.

(b) Station 25, θ = 270° **at** M_∞ = 0.80.

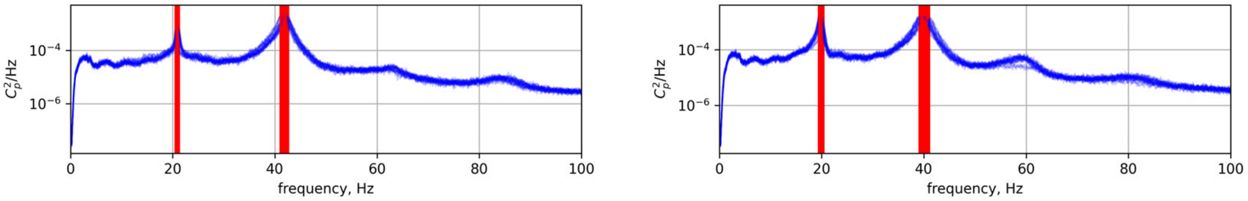

(c) Station 25, θ = 90° **at** M_∞ = 0.85.

(d) Station 25, θ = 270° **at** M_∞ = 0.85.

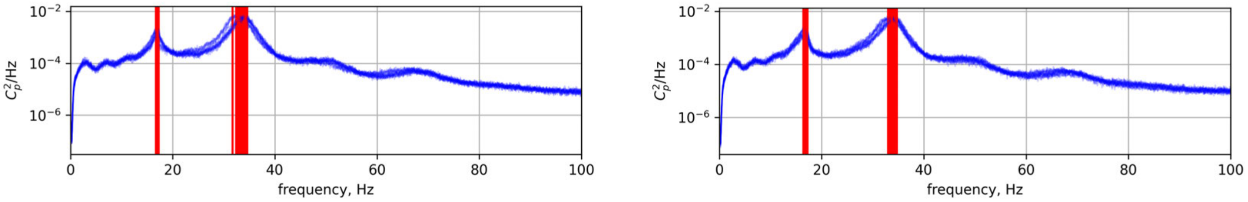

(e) Station 25, θ = 90° **at** M_∞ = 0.90.

(f) Station 25, θ = 270° **at** M_∞ = 0.90.

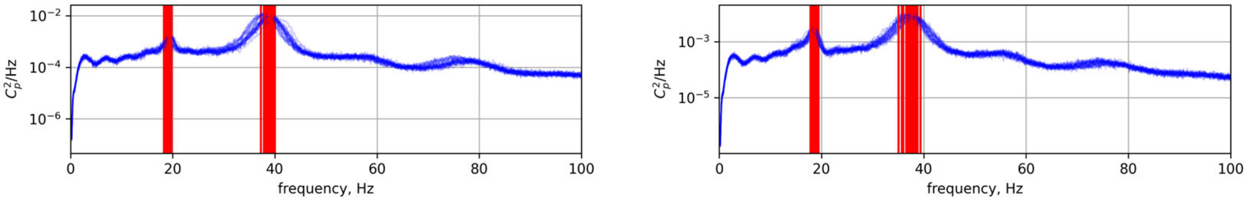

(g) Station 25, θ = 90° **at** M_∞ = 0.95.

(h) Station 25, θ = 270° **at** M_∞ = 0.95.

Fig. 13 C_p' **narrowband spectral peaks repeatability for PTs on the booster plane and located downstream of the booster FAH during Test 645.**

B. Comparison of Fluctuating Pressures, WT Test to Test

In this section, the repeatability analysis is extended to compare test-to-test data for repeat points during Test 645, Test 668, ATAT, and AUAT. In Fig. 17, the comparison core analysis stations are represented on the SLS configurations tested during each WT test, and in Fig. 18, data are presented for PTs at core stage comparison stations for these tests. Stations 24 and 27 have been added for additional context, station 32 on the engine section is compared, instead of station 33, to better match PT locations between tests, and azimuthal locations are chosen to match PTs between all tests. For this figure, all repeat data for each test and for each condition are combined and the mean $C'_{p,\mathrm{rms}}$ and 95% bounds are compared, corresponding to the blue lines in Fig. 8.

At station 16 (Fig. 18a), both Test 645 and ATAT have elevated $C'_{p,\mathrm{rms}}$ levels at M_∞ = 0.85 due to the shock-boundary layer interaction unsteadiness associated with the normal shock downstream of the CCJ. High-speed shadowgraph images from ATAT in Fig. 19 illustrate the shock footprint at M_∞ = 0.85 and the downstream movement of the shock (away from the sensor position at station 16) at M_∞ = 0.90. For Test 668 and AUAT, the WT models tested were Block 1B configurations (seen in Fig. 17), which has a longer forebody than the Block 1 configurations and shift the shoulder of the upper stage adapter forward. Thus, the shock-boundary layer interaction unsteadiness is not present at station 16 during those tests. For the higher M_∞ conditions shown in Fig. 18a, Test 645 has higher unsteadiness relative to the other tests, which are generally comparable, possibly because the combined effects of the expansion corner at the aft end of the LVSA and LAS nozzle wake (not present in the Block 1 cargo model tested during ATAT).

At stations 24, 25, and 27 (Figs. 18b–18d), $C'_{p,\mathrm{rms}}$ amplitudes generally compare well for tests in the same facility,

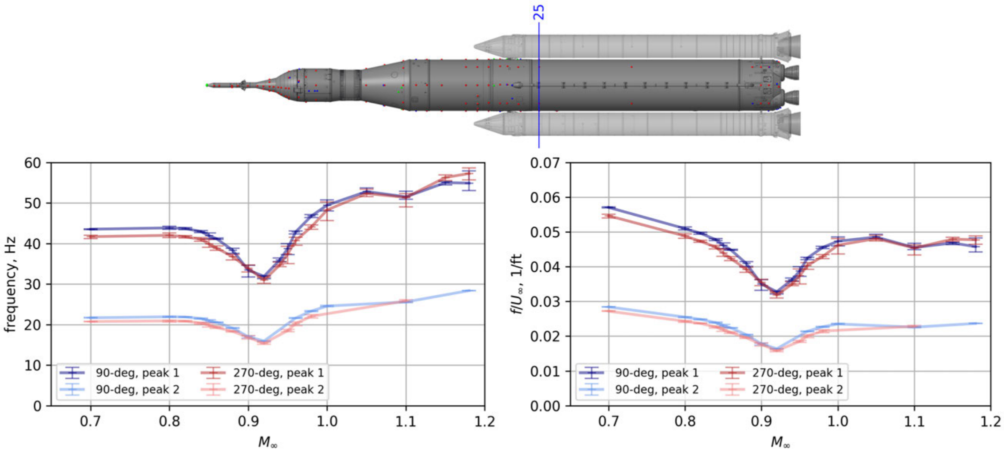

(a) Peak frequencies. **(b) Peak frequencies normalized by velocity.**

Fig. 14 Comparison of peak frequencies versus M_∞ at PTs downstream of the FAH at $\alpha = \beta = 0°$ for sensors on the booster plane of the core ($\theta \in \{90°, 270°\}$) for data acquired during Test 645.

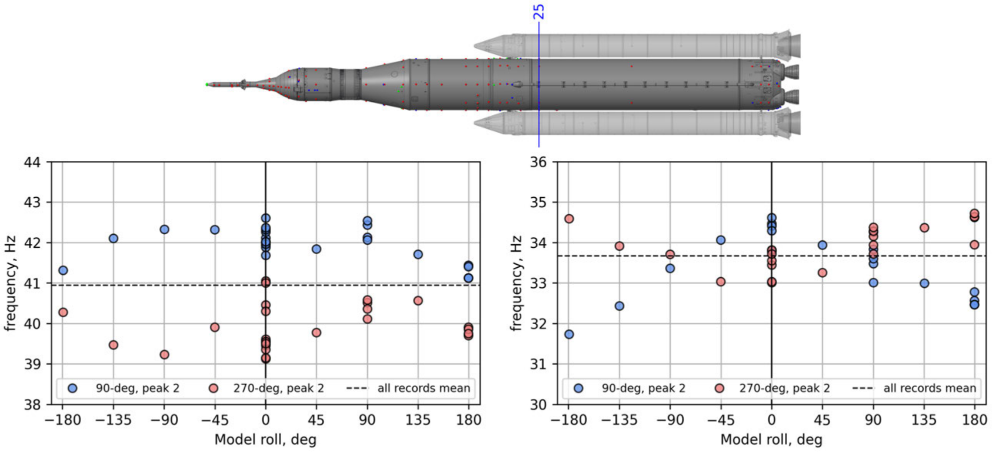

(a) $M_\infty = 0.85$. **(b)** $M_\infty = 0.90$.

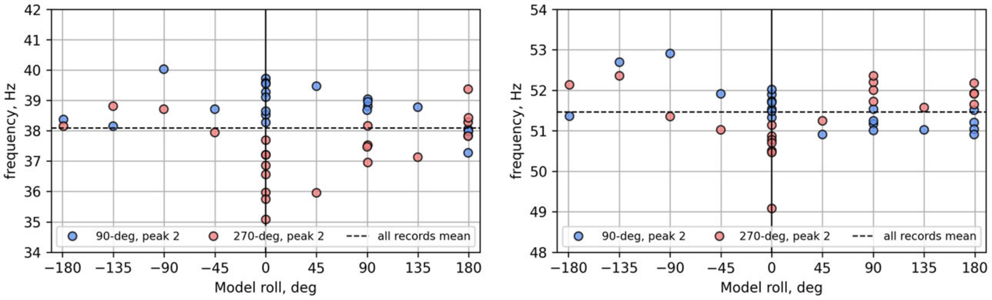

(c) $M_\infty = 0.95$. **(d)** $M_\infty = 1.10$.

Fig. 15 Peak frequencies versus model roll angle for PTs located downstream of the FAH and $\alpha = \beta = 0°$ for data acquired during Test 645.

but are often quite different for tests at different facilities. For example, at station 25 (Fig. 18c), for the lower M_∞ presented the ATAT and AUAT unsteadiness is 25% to 50% higher than the Test 645 and Test 668 data. At $M_\infty = 1.18$, however, the opposite is true. These data suggest that between models or facilities, the spatial extent of the peak

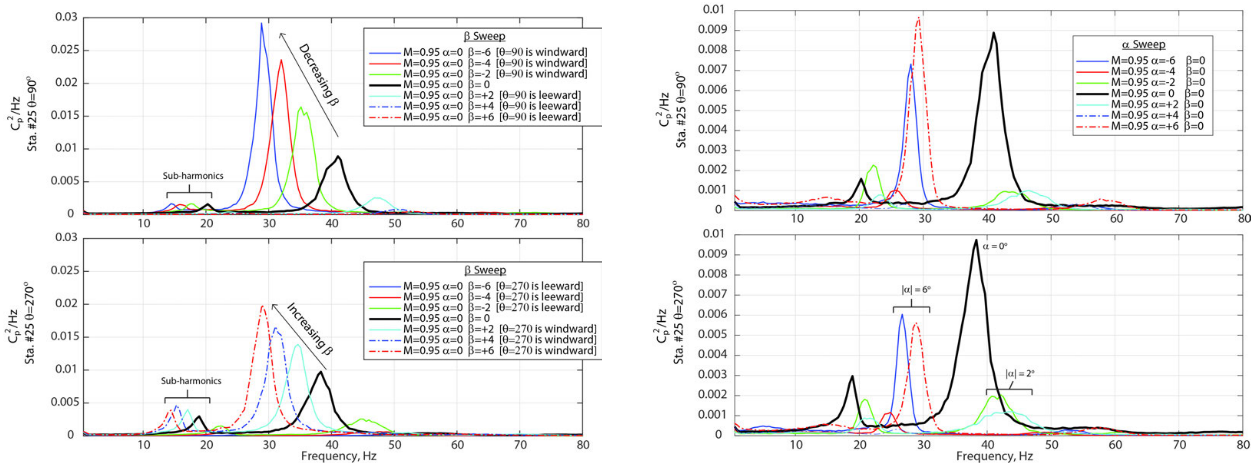

(a) $\alpha = 0°$ **and** β **sweep between ±6°.**

(b) α **sweep between ±6° and** $\beta = 0°$**.**

Fig. 16 PSDs measured during Test 645 at $M_\infty = 0.95$ **for PTs on core at** $\theta = 90°$ **facing the LSRB and at** $\theta = 270°$ **facing the RSRB downstream of booster FAH.**

unsteadiness downstream of the booster FAH may differ, with PTs at matched locations measuring the moving peak unsteadiness at different conditions. Farther aft at station 32 (Fig. 18e), all WT data compare well at the conditions shown. Based on these data, in the multibody region of the vehicle, where comparisons between facilities and tests are most applicable due to the wide variety of forebodies that have been tested, there are differences in the $C'_{p,\mathrm{rms}}$ amplitudes between facilities. Data for tests at the same facility, however, appear to be broadly similar.

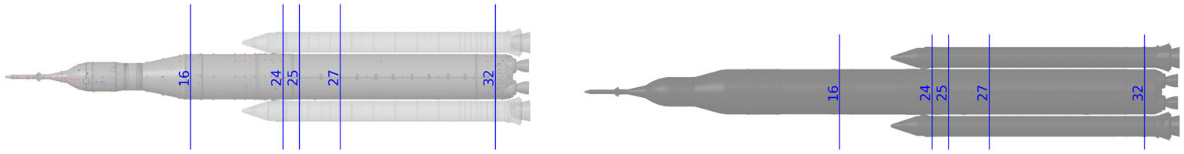

(a) Test 645, Block 1 crew.

(b) Test 668, Block 1B crew.

(c) ATAT, Block 1 cargo.

(d) AUAT, Block 1B cargo.

Fig. 17 Core analysis stations for test-to-test comparisons.

Next, sensor spectra data are presented to compare test-to-test repeatability. Two regions of the vehicle are dominated by spectral peaks in C'_p: (1) the region downstream of the booster FAH as previously discussed, and (2) the region downstream of the LAS nozzles on the MPCV. Using four sensors located at station 5 for the Block 1 (B1) configuration (and the corresponding station at the same distance from the LAS nozzles for tests of the Block 1B (B1B) configuration), Fig. 20 presents peak frequencies associated with the LAS nozzle shedding for data from Test 645, Test 668, and AUAT. Both Test 668 and AUAT tested the Block 1B crew configuration, with AUAT testing only the forebody at 4% scale (all WT test articles are shown in Fig. 2). For Test 668, data acquired during the air checkout portion of testing are also included for comparison. The mean spectral peaks correspond quite well between tests, while there are rather large bounds for the maximum and minimum spectral peaks. A significant contributor to this within-test variability is the different sensor location clocking angles relative to the LAS nozzles as well as the broad character of the LAS nozzle peak. Figure 20b presents the same data with frequencies normalized by the freestream velocity, U_∞, which indicates relatively constant reduced frequencies within this M_∞ range. Overall, the test-to-test comparisons indicate good agreement for peak spectral frequencies corresponding to the LAS nozzle shedding, with no notable differences observed between the Test 668 air and heavy gas data.

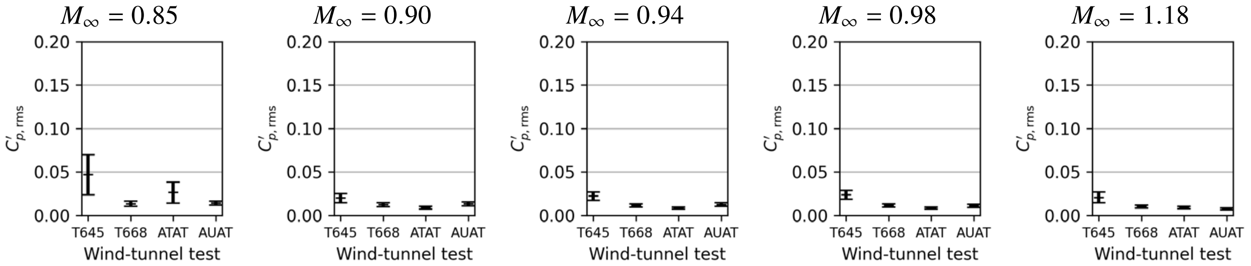

(a) Station 16, $\theta = 90°$**.**

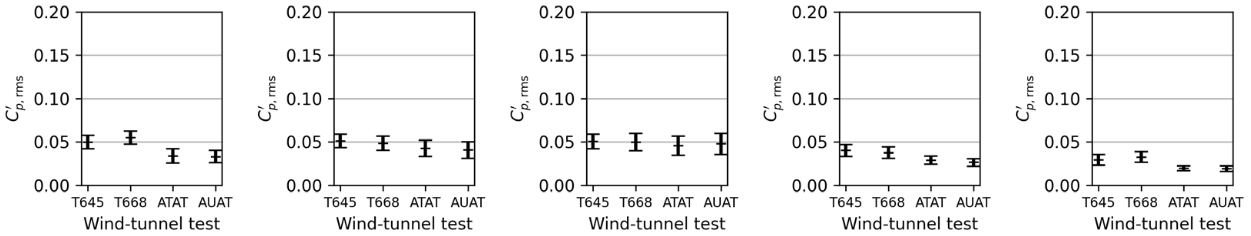

(b) Station 24, $\theta = 90°$**.**

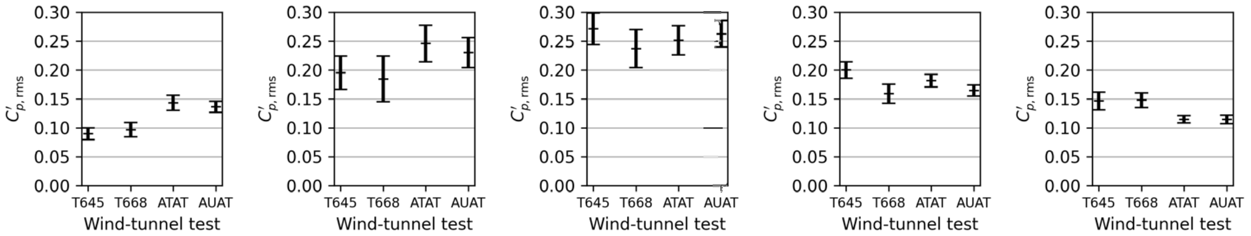

(c) Station 25, $\theta = 90°$**.**

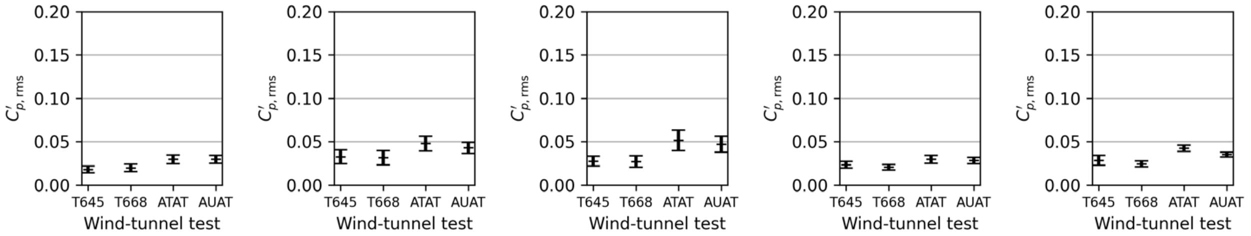

(d) Station 27, $\theta = 90°$**.**

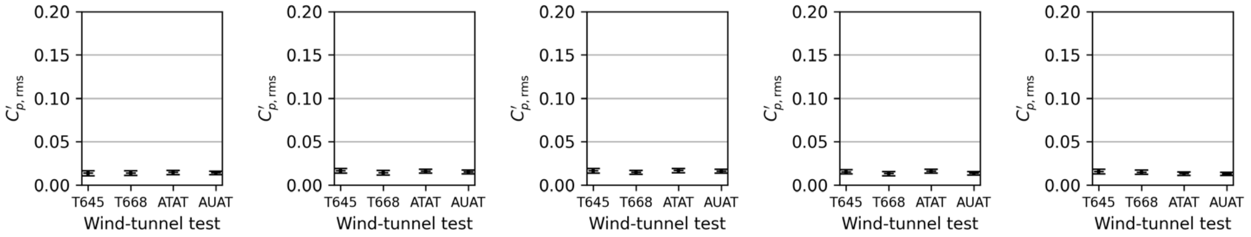

(e) Station 32, $\theta = 135°$**.**

Fig. 18 $C'_{p,\mathrm{rms}}$ **test-to-test repeatability during Test 645, Test 668, ATAT, and AUAT for PTs located at the core analysis stations for** $M_\infty = 0.95$ **and** $\alpha = \beta = 0°$**.**

For the region downstream of the booster FAH, Fig. 21 presents the narrowband spectral peaks identified for Test 668, ATAT, and AUAT. Similar to the results presented for Test 645, for most M_∞, there is an offset between the peaks identified for the LSRB-facing ($\theta = 90°$) and RSRB-facing ($\theta = 270°$) sensors in these data, appearing relatively largest for Test 668 and ATAT. Peaks up to $M_\infty = 1.40$ are presented for the two tests at UPWT, which in the

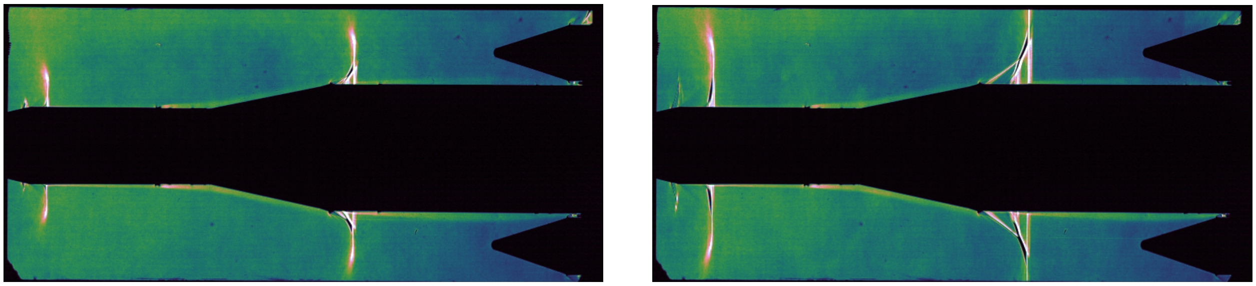
(a) $M_\infty = 0.85$. (b) $M_\infty = 0.90$.

Fig. 19 High-speed shadowgraph pixel variance images acquired during ATAT indicating regions of high flow unsteadiness.

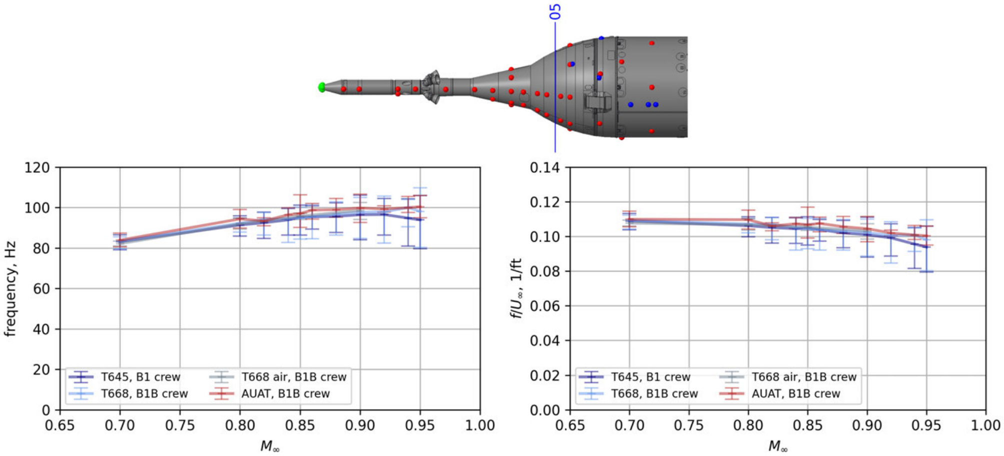

(a) Peak frequencies. **(b) Peak frequencies normalized by velocity.**

Fig. 20 Comparison of peak frequencies versus M_∞ at PTs downstream of the LAS nozzles at $\alpha = \beta = 0°$ for several WT tests.

velocity-normalized curves in Figs. 21b and 21c indicate the region of relatively flat reduced frequencies extends for $M_\infty \in [1.00, 1.40]$. Only the higher frequency peak is plotted in the ATAT and AUAT figures as the lower frequency peak is either not measured at this PT location or not extracted using the peak picking parameters utilized.

In Fig. 22, a summary of the narrowband peak frequencies identified in the C_p' spectra for all the WT tests are presented. Data from the Test 668 air runs and the ATAT 9x7 SWT runs have been added in addition to the data presented above, and the ATAT 11-Ft TWT runs after unsteady pressure sensitive paint (uPSP) was applied have been separated from the remainder of the unpainted model ATAT runs. While there are small differences in the peak frequencies between the unpainted and painted ATAT WT test points ("ATAT, B1 cargo" versus "ATAT, B1 cargo uPSP"), painting the model and thus changing the surface roughness slightly does not appear to affect the peak shedding frequency significantly in the region downstream of the FAH.

During Test 668, limited data were acquired in air, which, up to $M_\infty = 0.90$, do indicate notable differences in peak shedding frequency relative to the comparison Test 668 data conducted in heavy gas ("T668 air, B1B crew" versus "T668, B1B crew" in Fig. 22). For sensors facing the LSRB and RSRB (Figs. 22a and 22b), the air run peaks are consistently lower than that for heavy gas by ≈ 3 Hz. For the higher Re_D heavy gas test points at $M_\infty = 0.90$, the mean $Re_D = 6.03$ based on core diameter is a factor of approximately 6 larger than the mean $Re_D = 1.08$ for the air run data points, which, along with possible test medium effects, may be part of the explanation for systematic differences. There are also notable differences in peak frequencies on both sides of the core between the AUAT and ATAT tests for $M_\infty > 0.98$. While there were some minor geometry changes to the WT models between these tests farther aft on the boosters (addition of booster field joints farther downstream), the only major change is the difference in forebody (Block 1B cargo for AUAT and Block 1 cargo for ATAT). Other potential sources of these differences may be test-to-test

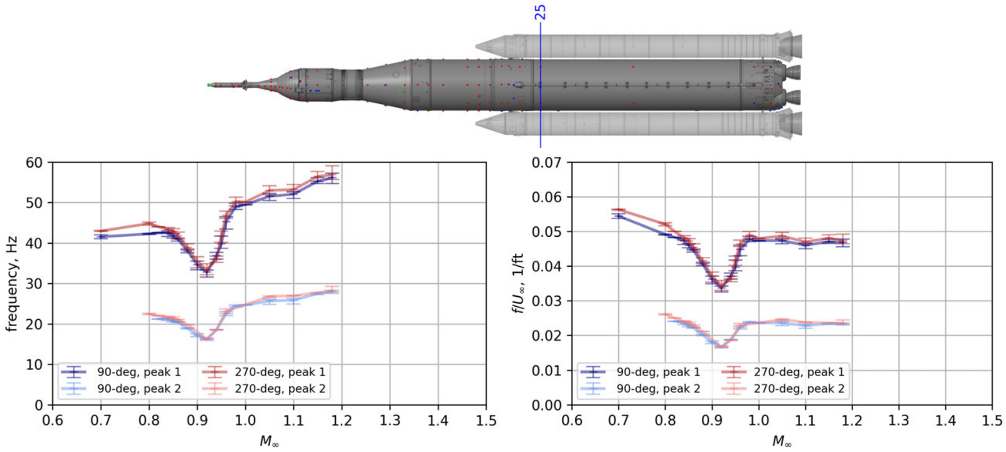

(a) Test 668.

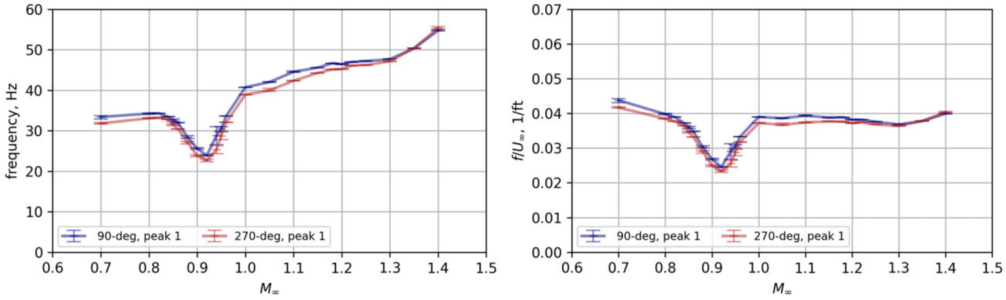

(b) ATAT.

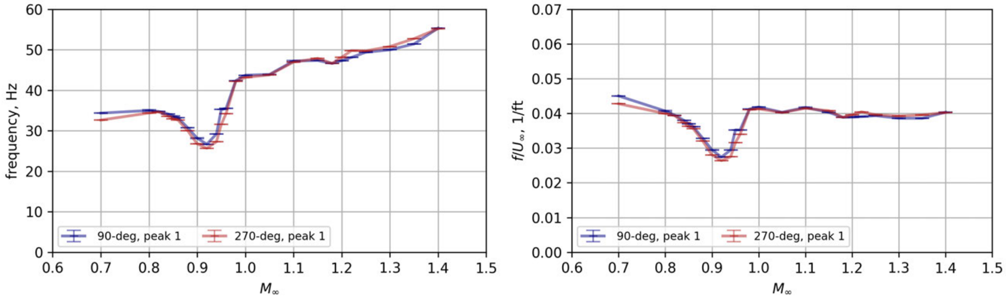

(c) AUAT.

Fig. 21 Comparison of peak frequencies versus M_∞ at $\alpha = \beta = 0^\circ$ for PTs downstream of the FAH on the booster plane of the core ($\theta \in \{90^\circ, 270^\circ\}$). Figures in the left column present frequencies, and figures in the right column present velocity-normalized frequencies.

variability, small geometry differences, or installation orientation variability for the additively manufactured booster FAH protuberance.

The most significant differences in peak frequencies are between facilities, with the data for tests conducted at UPWT indicating significantly lower peak frequencies (by ≈8-10 Hz, for example, between TDT Test 645 and UPWT ATAT) than those conducted at TDT throughout the M_∞ range presented. Differences in model designs, such as the detailed geometry of the booster-to-core gap in this region or the booster FAH geometry, are the hypotheses currently under study using time-accurate CFD to investigate possible explanations for these peak frequency differences. Since the mean peak frequencies identified in the region downstream of the LAS nozzles, presented in Fig. 21, compare favorably between facilities, the consistent differences identified in the booster FAH region appear to be related to local geometry or flowfield differences in the multibody region of the vehicle. These differences in peak shedding frequency are of significant importance in the context of the flight data, to be presented in the next section, where the flight peak

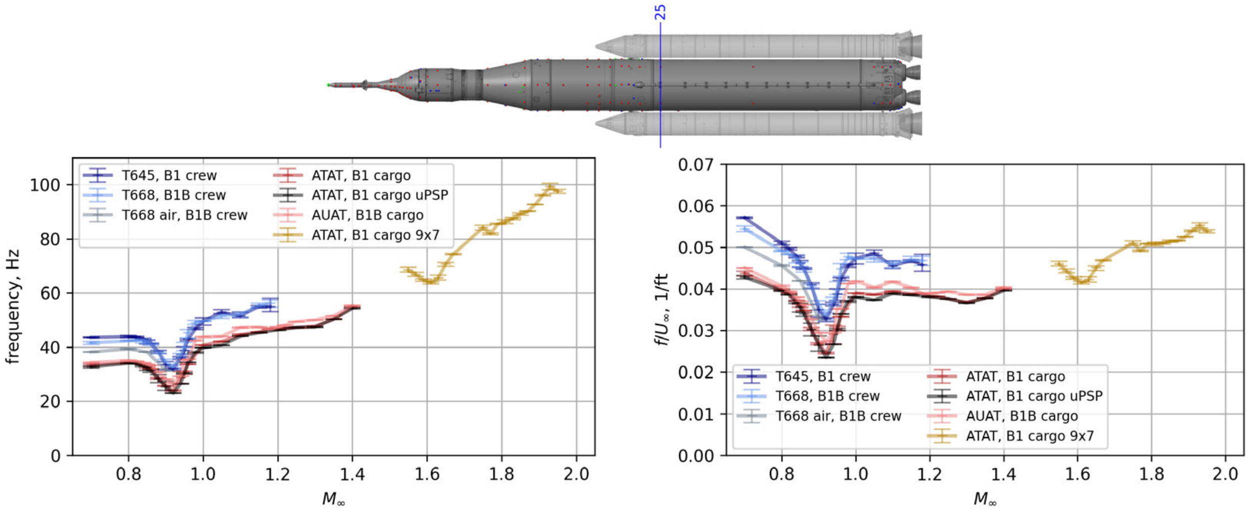

(a) Booster plane sensor on the core at θ = 90° (facing LSRB).

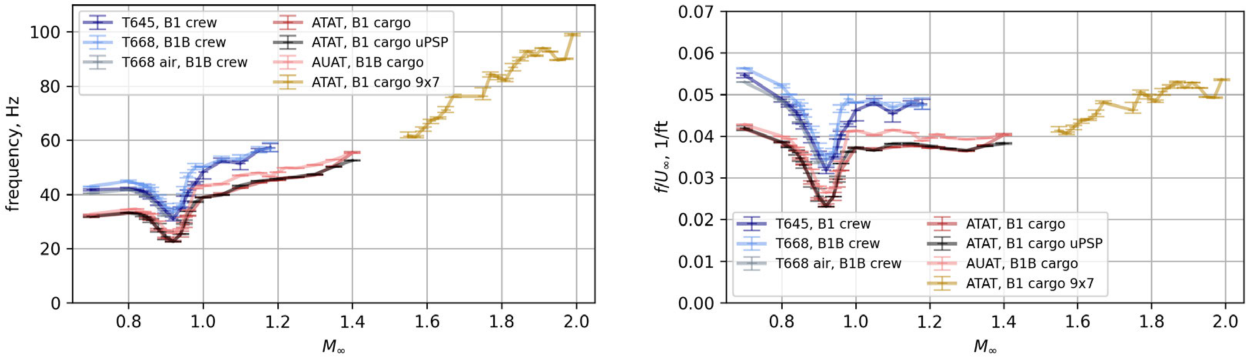

(b) Booster plane sensor on the core at θ = 270° (facing RSRB).

Fig. 22 Comparison of peak frequencies versus M_∞ at $\alpha = \beta = 0°$ for PTs downstream of the FAH for several WT tests. Figures in the left column present frequencies, and figures in the right column present velocity-normalized frequencies.

frequencies are shown to be closer to those identified in the tests conducted at UPWT. These observations have driven the computational studies described above, as well as WT model modifications to more accurately match the as-flown vehicle geometry for an upcoming test at TDT to determine how increasing the fidelity of the core stage geometry in the vicinity of the booster FAH changes the identified peak frequencies. As has been shown in several previous tests, the unsteady pressure field is sensitive to the geometry in this region [14].

C. Comparison of Fluctuating Pressures, Flight to WT

In this section, results are presented comparing the unsteady pressure environments measured during the Artemis I flight to preflight WT tests. In Fig. 23, the vehicle attitude based on the BET for Artemis I is shown versus M_∞. Throughout this portion of ascent, the vehicle α_{total} is relatively low, which provides some support for the applicability of the repeatability analyses described above for this flight despite the sensitivity of fluctuating pressure environments to vehicle orientation. Most of the WT results shown below will be for points that best match the flight conditions and vehicle attitudes, but results from the repeatability analyses described above will also be referenced for context.

Figure 24 compares distributions of $C'_{p,\text{rms}}$ for several M_∞ using Test 645 matched conditions and data from the Artemis I flight. A uniformly distributed x-θ (unwrapped) grid is mapped to the nearest sensor data in these figures, providing a broad look at the spatial distribution of unsteady pressures. This overview, where relatively local regions of increased $C'_{p,\text{rms}}$ are present downstream of the booster FAH, illustrates the importance of that region on core stage and booster unsteady pressure environments during transonic flight. In addition, the relative sparsity of instrumentation in

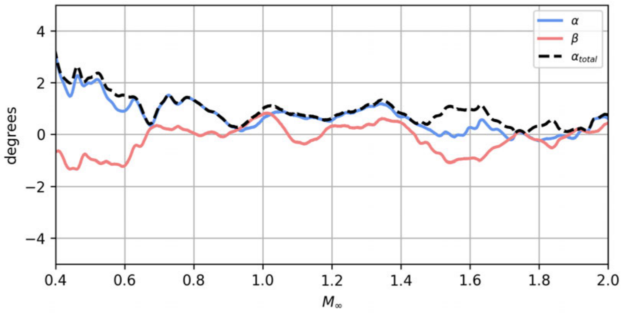

Fig. 23 Artemis I attitude from the BET.

this region on the Artemis I flight vehicle in comparison to the WT RBM illustrates the challenge of characterizing this environment using flight data and assessing the accuracy of preflight WT test environments. One notable feature is that the $M_\infty = 0.80$ condition is the only matched WT point presented in this figure where the attitude parameters are nonzero – for this condition, the matched point attitude is $\alpha = 1.02°$. With the high sensor density on the RBM, the change in $C'_{p,\mathrm{rms}}$ spatial distribution is visible, with the wake of the booster FAH rotating away from the windward lower surface of the model ($\theta = 180°$). For the other cases shown here, the wake unsteadiness is oriented directly aft in the WT distributions. Due to sensor density limitations on the flight vehicle, these characteristics are not easily identified, which serves as a reminder that the observability of peak unsteady environments is strongly related to sensor location.

In Fig. 25, azimuthal slices of these $C'_{p,\mathrm{rms}}$ distributions are presented for several M_∞ and for clocking angles $\theta = \{0°, 90°\}$. For the WT data, the ensemble mean as well as the KDE of the corresponding moving $C'_{p,\mathrm{rms}}$ windows of the matched point are plotted. For the $\theta = 0°$ slice, the tunnel and flight data match well for all M_∞ presented here, to include matching the increase in unsteadiness downstream of the LVSA CCJ. The largest qualitative difference appears at $M_\infty = 0.90$ for station 8, where the tunnel data indicate a relatively high unsteadiness and variability, while the comparison flight sensor, slightly aft, is relatively quiet. This difference is related to the high unsteadiness associated with a normal shock that travels downstream as M_∞ increases on this segment of the vehicle, and which was positioned close to this sensor during the tunnel test at $M_\infty = 0.90$. As will be shown below, the high unsteadiness associated with that normal shock oscillating fore and aft of the sensor position does not appear in the flight data, where the shock travels monotonically downstream during ascent.

For the $\theta = 90°$ slice on the vehicle forebody, the trends and magnitudes match well between flight and tunnel. At the beginning of the booster nose cones, flight magnitudes appear somewhat increased relative to the tunnel data for $M_\infty \geq 0.85$. Due to the relative sparsity of sensors on the flight vehicle, the trends downstream of the booster FAH, where the pressure field unsteadiness is largest, are more difficult to compare. It is clear, however, that the flight data at matched sensor stations on the booster plane do not match the WT data as well as in other regions of the vehicle. Based on the three flight sensors located in this region of the vehicle, compared to the tunnel data it appears that one or several characteristics may be true during flight: (1) $C'_{p,\mathrm{rms}}$ magnitudes are generally higher, (2) $C'_{p,\mathrm{rms}}$ peak may occur further downstream, and (3) longitudinal extent of elevated $C'_{p,\mathrm{rms}}$ may be larger. Any one or combination of these may be true, depending on assumptions related to the shape of the flight and tunnel $C'_{p,\mathrm{rms}}$ distributions, which even for the tunnel data is not highly resolved. Uncertainties associated with the magnitudes and spatial extent of high unsteadiness in this region are significantly important due to the high coherence of the unsteady pressure modes associated with the booster FAH wake and the relatively low frequencies associated with those modes that may interact with vehicle structural modes. Better understanding of this vehicle region both in subscale tests and the next launch are high priorities.

The remainder of this section will present results focusing on the analysis stations shown in Fig. 4. Comparisons of flight and tunnel data are shown in Fig. 26 for stations 4 and 8, located on the LAS and SM. In the top row of the figures, $C'_{p,\mathrm{rms}}$ versus M_∞ is plotted with comparison tunnel data including: (1) KDEs for ensembles of the matched condition test point from Test 645, (2) the mean of that ensemble, and (3) maximum and minimum mean $C'_{p,\mathrm{rms}}$ for all $\alpha = \beta = 0°$ repeats acquired at each M_∞. Although the vehicle attitude throughout its ascent was not $\alpha = \beta = 0°$, these repeat cases give an indication of how variable the matched WT point mean $C'_{p,\mathrm{rms}}$ would likely be if repeats were available at the matched attitudes. For both of these stations, the flight data correspond reasonably well with the matched tunnel data, particularly in light of the mean $C'_{p,\mathrm{rms}}$ dispersions indicated by the repeat data and the moving window distributions plotted with the KDEs. For station 8, the high tunnel $C'_{p,\mathrm{rms}}$ at $M_\infty = 0.90$ is related to the normal shock that, oscillating fore and aft of this sensor during Test 645, led to high unsteadiness. During flight, however, the

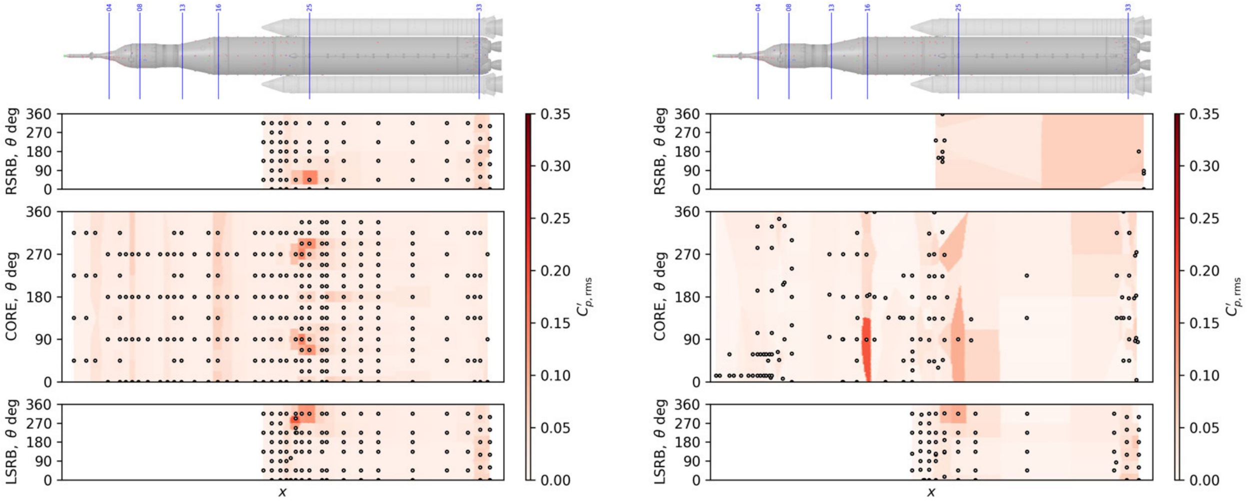

(a) M_∞ = 0.80**, tunnel.** **(b)** M_∞ = 0.80**, flight.**

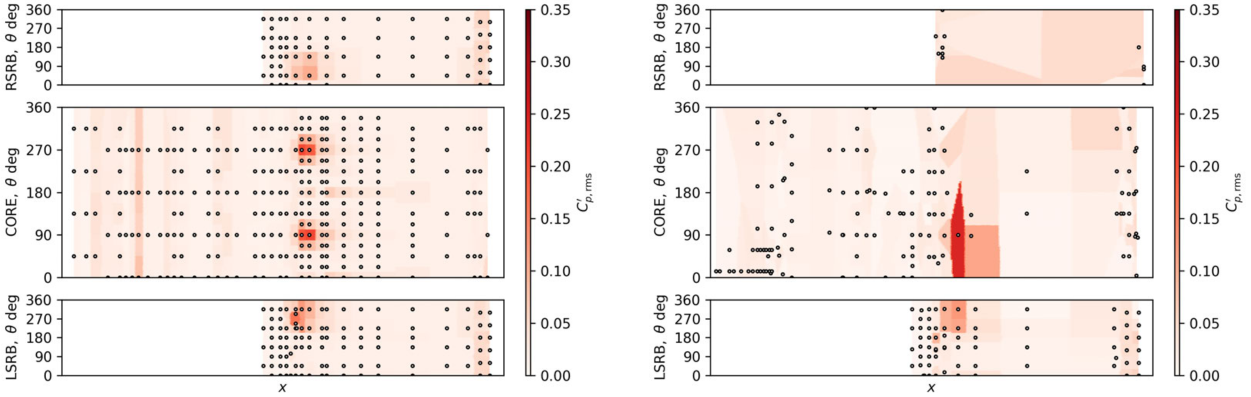

(c) M_∞ = 0.90**, tunnel.** **(d)** M_∞ = 0.90**, flight.**

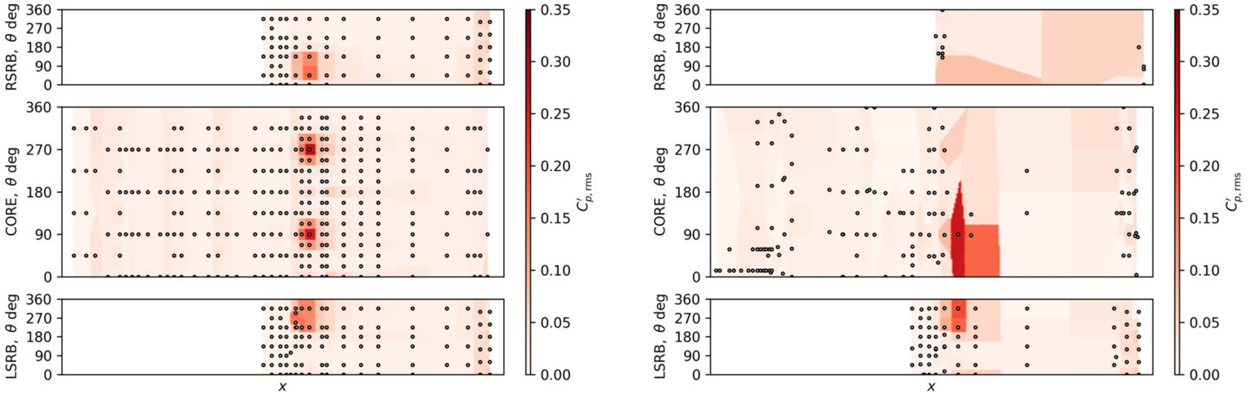

(e) M_∞ = 0.95**, tunnel.** **(f)** M_∞ = 0.95**, flight.**

Fig. 24 Unwrapped $C'_{p,\mathrm{rms}}$ distributions based on Test 645 and flight data for increasing M_∞.

shock passed over this station at approximately that same M_∞, but did not oscillate, so the flight magnitudes dropped to the levels measured in the tunnel data after the shock has moved past that sensor.

The spectrograms of flight C'_p, shown in the second row of figures, both indicate the increasing peak frequency associated with LAS nozzle shedding. Comparisons of this peak frequency will be made with the tunnel predicted peaks below. In the remaining plots in Fig. 26, global continuous wavelet transform (CWT) spectra of the flight sensors

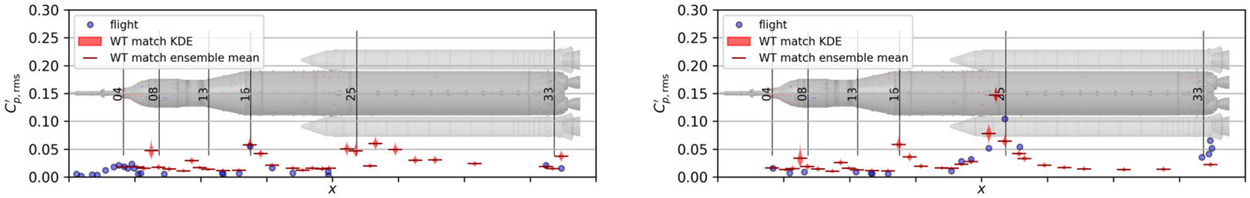

(a) $M_\infty = 0.80$**, PTs located along** $\theta = 0°$**.**

(b) $M_\infty = 0.80$**, PTs located along** $\theta = 90°$**.**

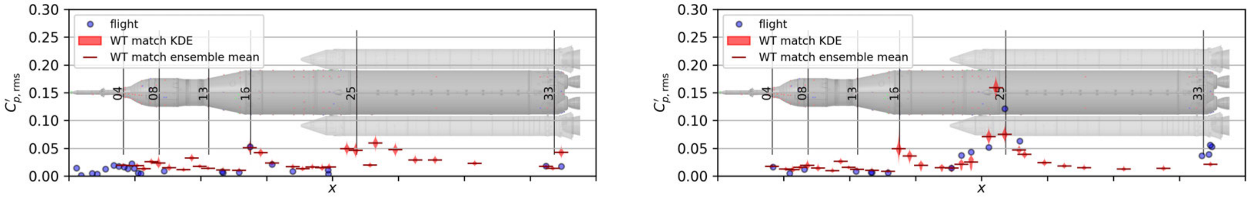

(c) $M_\infty = 0.85$**, PTs located along** $\theta = 0°$**.**

(d) $M_\infty = 0.85$**, PTs located along** $\theta = 90°$**.**

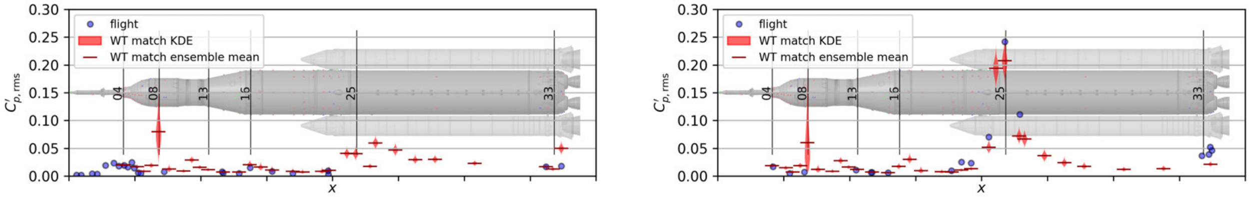

(e) $M_\infty = 0.90$**, PTs located along** $\theta = 0°$**.**

(f) $M_\infty = 0.90$**, PTs located along** $\theta = 90°$**.**

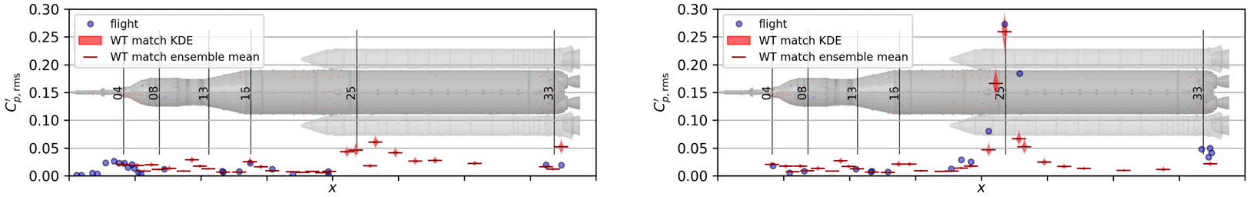

(g) $M_\infty = 0.95$**, PTs located along** $\theta = 0°$**.**

(h) $M_\infty = 0.95$**, PTs located along** $\theta = 90°$**.**

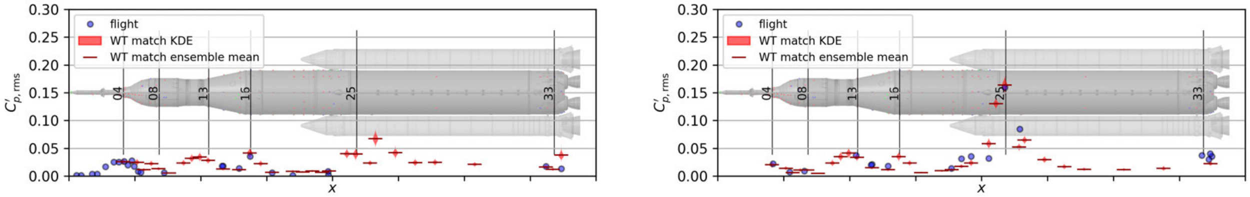

(i) $M_\infty = 1.05$**, PTs located along** $\theta = 0°$**.**

(j) $M_\infty = 1.05$**, PTs located along** $\theta = 90°$**.**

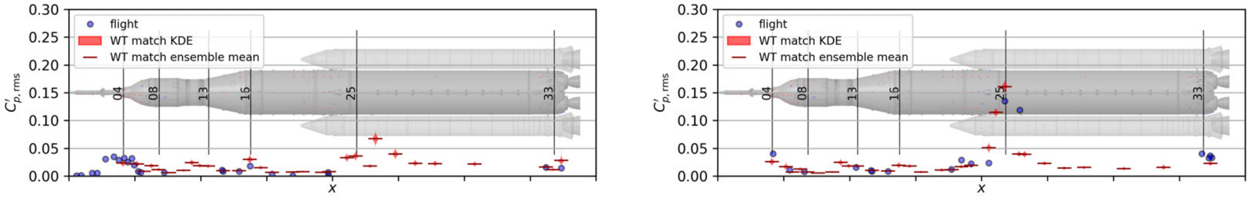

(k) $M_\infty = 1.15$**, PTs located along** $\theta = 0°$**.**

(l) $M_\infty = 1.15$**, PTs located along** $\theta = 90°$**.**

Fig. 25 Comparison of $C'_{p,\mathrm{rms}}$ **longitudinal distribution between Test 645 and flight.**

are presented in comparison to tunnel global CWT spectral bounds. The global CWT is calculated as the time average of the CWT over a specified window (here, 0.5 s full-scale window durations), and several WT quantiles are formed for the ensemble global CWTs calculated for matched points. The red curve in each figure corresponds to the tunnel ensemble mean spectrum, and the red areas correspond to quantile ranges containing the percentage of the ensemble

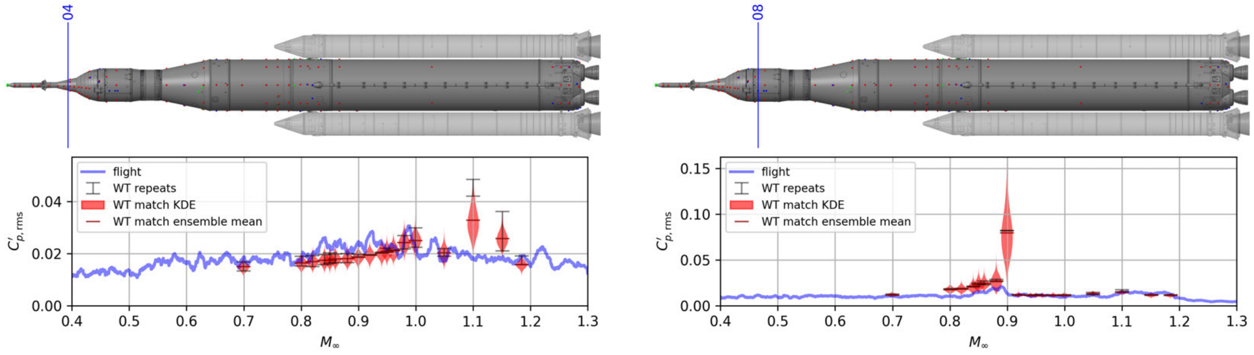

(a) $C'_{p,\mathrm{rms}}$**.** **(f)** $C'_{p,\mathrm{rms}}$**.**

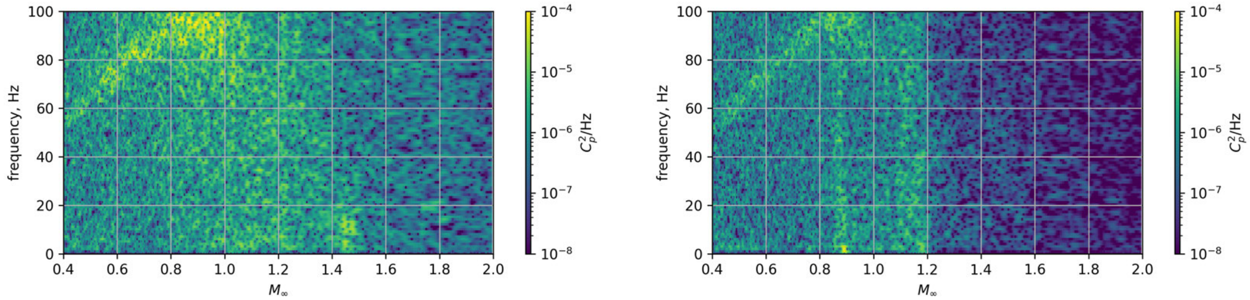

(b) C'_p **spectrogram.** **(g)** C'_p **spectrogram.**

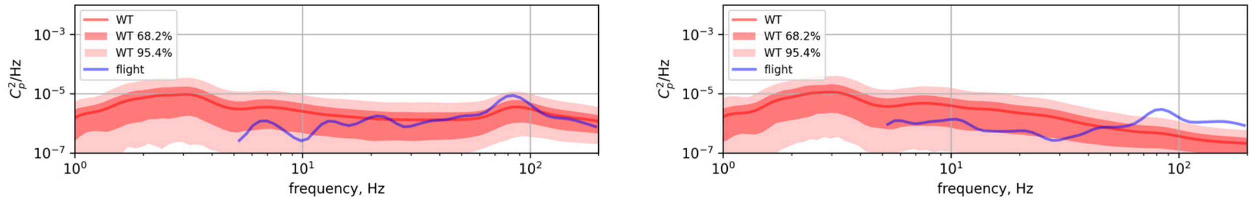

(c) Global CWTs, $M_\infty = 0.70$**.** **(h) Global CWTs,** $M_\infty = 0.70$**.**

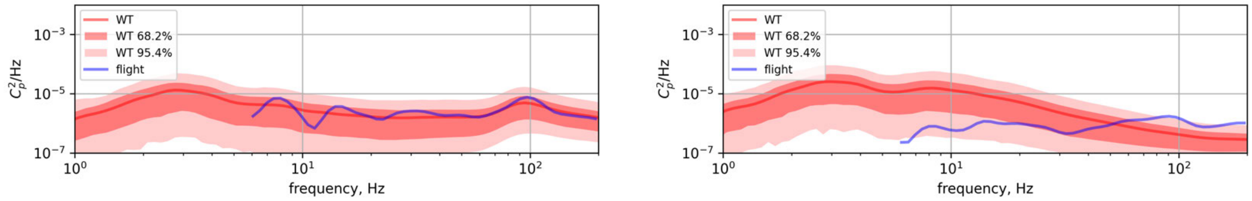

(d) Global CWTs, $M_\infty = 0.80$**.** **(i) Global CWTs,** $M_\infty = 0.80$**.**

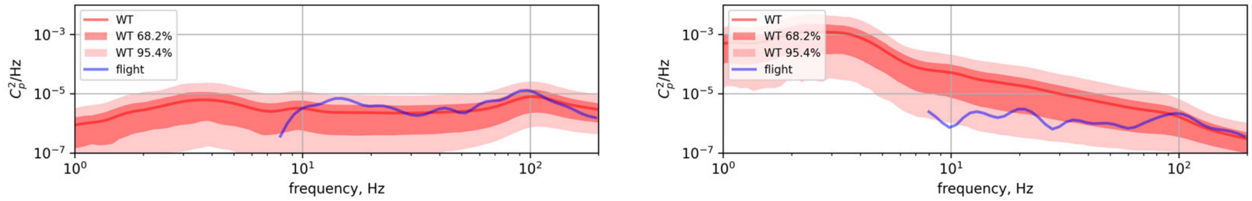

(e) Global CWTs, $M_\infty = 0.90$**.** **(j) Global CWTs,** $M_\infty = 0.90$**.**

Station 4, flight PT located at $\theta = 58.3°$**, WT matched PT located at** $\theta = 90°$**.**

Station 8, flight PT located at $\theta = 330°$**, WT matched PT located at** $\theta = 0°$**.**

Fig. 26 Artemis I flight data compared to WT data from Test 645 for analysis stations on the LAS and MPCV.

specified in the legend. For the station 4 sensor comparisons, the tunnel bounds plotted contain the flight spectra well, and as will be shown in more detail below, the flight spectral peak frequency matches the tunnel data well. For station 8, the comparisons are reasonable in the lower frequencies, with the flight spectra generally lower than the tunnel ensemble spectra. However, for the higher frequencies plotted, the flight spectra exceed the WT bounds at $M_\infty = 0.70$ and 0.80. This is caused by the influence of the LAS nozzle wake, which is observable as a peak in the flight spectra but not present in the WT spectra. In this case, the difference is due to a difference in sensor location between flight and tunnel: the flight sensor is located at $\theta = 330°$, while the closest matched WT sensor is located at $\theta = 0°$. Since the LAS nozzles are clocked at $\theta \in \{58.3°, 148.3°, 238.3°, 328.3°\}$, the 30° of separation between these "closest-matched" sensors brings the tunnel sensor outside the dominant wake of the upstream LAS nozzle. Considering the flight sensor located at $\theta = 90°$ at this same longitudinal station, the dominant frequency peaks identifiable in the spectrogram in Fig. 26g are not present in the spectrogram for this sensor in Fig. 27, as this flight sensor is azimuthally separated from the dominant wake of the upstream LAS nozzles by approximately the same angle as the tunnel sensor above. This example is illustrative of sensor location sensitivity on measured unsteadiness in the presence of nonspatially uniform pressure fields.

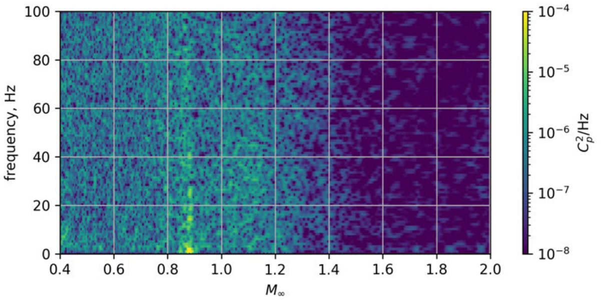

Fig. 27 C_p' spectrogram for sensor located at station 8, $\theta = 90°$.

Figure 28 provides comparisons of the spectrogram for flight sensors at station 4 and the mean peak frequencies for three WT tests (from Section IV.B). Throughout the M_∞ range, the peak frequencies compare well with the flight spectrogram, particularly considering that the flight attitude was continuously varying during ascent and the tunnel data presented are for the $\alpha = \beta = 0°$ repeatability analyses. Similar results have been shown for LAS nozzle peak frequency matching between tunnel and flight for the Ares I-X flight test vehicle [11].

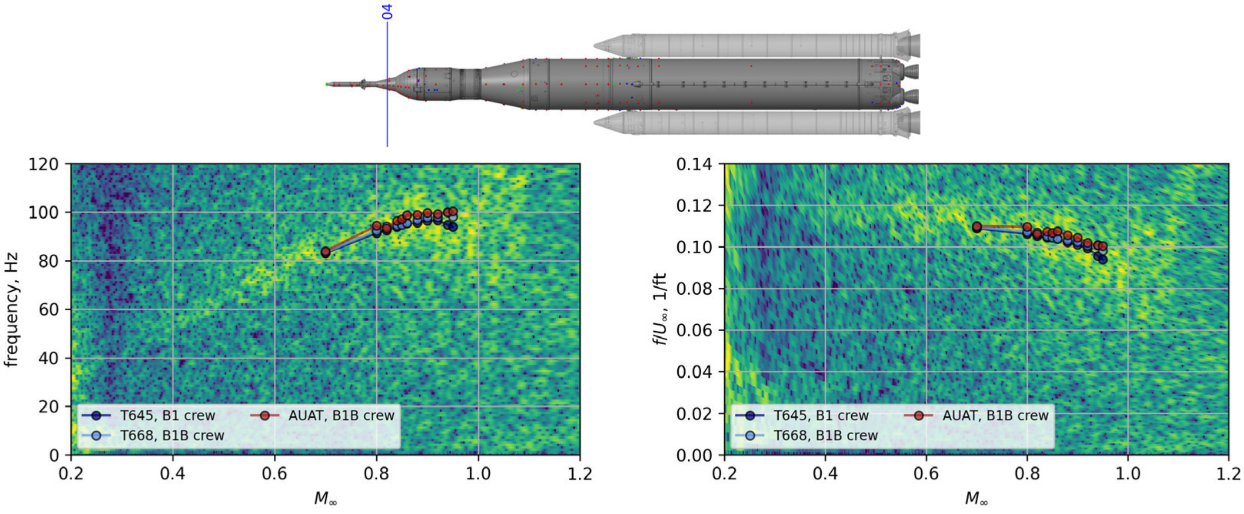

(a) Peak frequencies.

(b) Peak frequencies normalized by velocity.

Fig. 28 Comparison of peak frequencies from WT tests versus M_∞ at PTs downstream of the LAS nozzles. WT data are overlaid on the flight data spectrogram for matched sensor location.

In Fig. 29, summary flight to tunnel comparisons for stations 13 and 16, located on the LVSA and forward skirt, are presented. For station 13, the $C'_{p,\mathrm{rms}}$ versus M_∞ trends in the flight curve are correspond well with the tunnel data, including the relatively increased unsteadiness in this recirculation region at lower supersonic M_∞. The global CWTs presented also match well between flight and tunnel. Generally similar conclusions can be drawn for the comparisons shown for station 16. In the $C'_{p,\mathrm{rms}}$ versus M_∞ plot, the tunnel data indicate high unsteadiness between $M_\infty = 0.85$ and 0.88 corresponding to the normal shock oscillating in the vicinity of this sensor position during the WT test points (shown in Fig. 19 for $M_\infty = 0.85$ during the comparable ATAT test). During flight, however, little evidence of shock oscillation is present in the data, with the shock transitioning aft over this sensor location and the unsteady pressure magnitudes decreasing to the reduced, attached boundary layer, levels at $M_\infty \approx 0.88$.

Comparisons are shown in Fig. 30 for two sensors on the booster plane located at station 24 on either side of the core. For both of these sensors, the tunnel data predicts relatively high transonic unsteadiness and large point-to-point variability in the ensemble $C'_{p,\mathrm{rms}}$ means as represented by the repeat upper and lower bounds. Generally, the $C'_{p,\mathrm{rms}}$ trend versus M_∞ compares well between flight and tunnel, with the exception of the peak centered at $M_\infty \approx 0.94$ in the flight data that is not measured in the tunnel data. In the spectrograms, the presence of the dominant unsteady pressure modes associated with the booster FAH wake are clear – comparisons to the previously identified tunnel peaks will be shown below. In the global CWTs, however, indications of differences between the WT and flight peaks are evident. Depending on M_∞, either one or both peaks are present, but for both sensors and for all M_∞ the peaks occur at lower frequencies relative to the tunnel data. The magnitudes of the spectra are generally comparable at and away from the peaks for these M_∞.

In Fig. 31, comparisons of the flight spectrograms and WT mean peak frequencies, for PTs at station 24, are summarized. For the tunnel data, only the higher frequency peak is plotted for all tests. While the general trends match between flight and tunnel, the flight peaks are much lower than those identified for tests conducted in the TDT and match closer to those tests conducted in UPWT. As discussed above, it is not known why the frequencies differ between facilities, but current work is underway to explore differences in WT RBM geometries in this region, as well as with the Artemis I as-built geometry.

Figure 32 summarizes flight comparisons to tunnel data for sensors on the booster plane at stations 25 and 75. At station 25, the flight $C'_{p,\mathrm{rms}}$ is higher than, or at, the upper bound of the tunnel data for $M_\infty \leq 0.92$, and at station 75, the flight $C'_{p,\mathrm{rms}}$ is higher for all M_∞. The major source of these differences is the increased magnitudes of the unsteady pressure modes associated with the booster FAH shedding during flight, as can be seen in the increased spectral magnitudes for these modes in the global CWT comparisons (where the same frequency shift down, relative to tunnel data, is also present). Based on these comparisons, and those shown in Fig. 25, it appears that the tunnel data do not accurately estimate the magnitude and/or the spatial extent of the increased pressure field unsteadiness in this region of the vehicle for a range of transonic and low supersonic M_∞.

Comparisons of the flight spectrograms and WT mean peak frequencies, for sensors at stations 25 and 75, are summarized in Fig. 33. As is the case for the comparisons at station 24, the flight peaks are much lower than those identified for tests conducted in TDT and match closer to those tests conducted in UPWT. At these stations, it is also clear that the increased magnitudes of the narrowband peaks persist into the supersonic flight conditions, particularly at station 75. These flight peaks are quite different than those identified during the ATAT test in the 9- by 7-ft test section and do not match the tunnel trend in reduced frequencies shown in Figs. 33c and 33f.

Figure 34 presents summary flight to tunnel comparisons for sensors at station 33, located on the engine section. For both sensors, the flight $C'_{p,\mathrm{rms}}$ are higher than the matched tunnel data for all M_∞. The flight spectrograms indicate that the frequency peak associated with the FAH wake is present even this far aft, and the global CWT comparisons show that this peak is also present in the tunnel data (albeit at a higher frequency as discussed above). However, the spectral peak magnitude associated with this unsteady pressure mode is larger in the flight data, and the higher frequency spectral magnitudes are significantly larger for the station 33 sensor located at $\theta = 315.35°$ compared to the WT spectral bounds. This broadband excitation increase is reflected in the $C'_{p,\mathrm{rms}}$ versus M_∞ comparison, and may be related to engine-on contributions not present in the tunnel data.

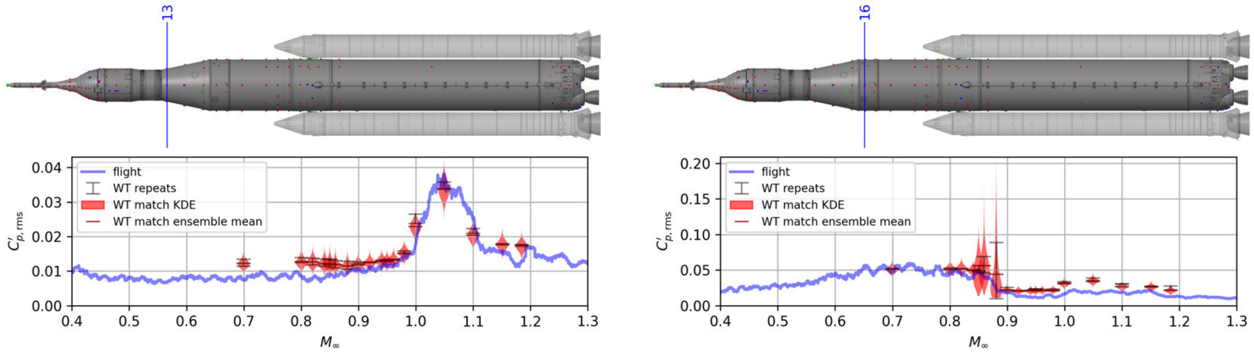

(a) $C'_{p,\text{rms}}$.

(f) $C'_{p,\text{rms}}$.

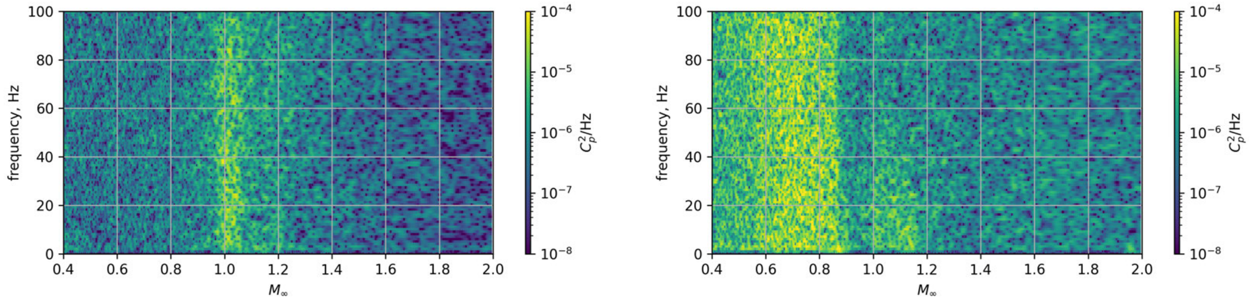

(b) C'_p spectrogram.

(g) C'_p spectrogram.

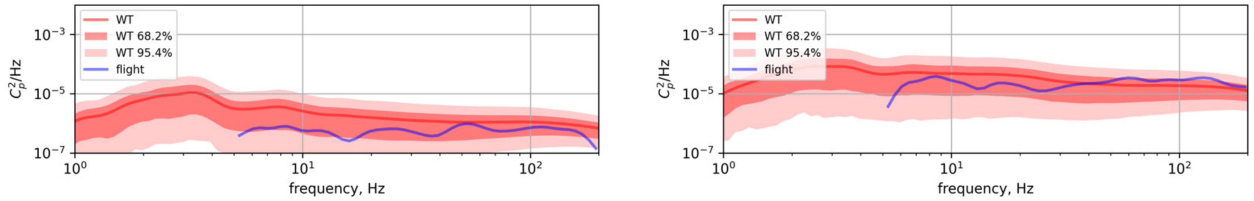

(c) Global CWTs, $M_\infty = 0.70$.

(h) Global CWTs, $M_\infty = 0.70$.

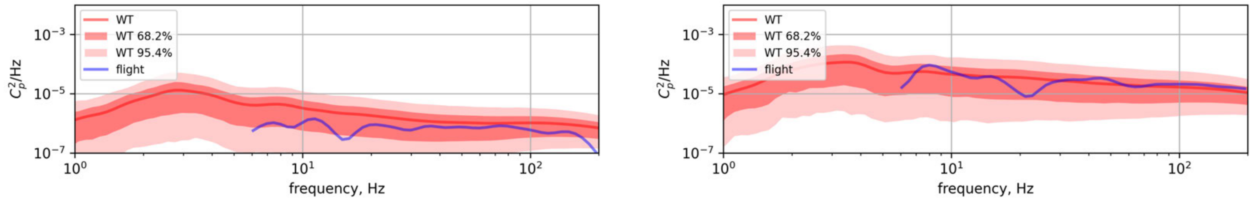

(d) Global CWTs, $M_\infty = 0.80$.

(i) Global CWTs, $M_\infty = 0.80$.

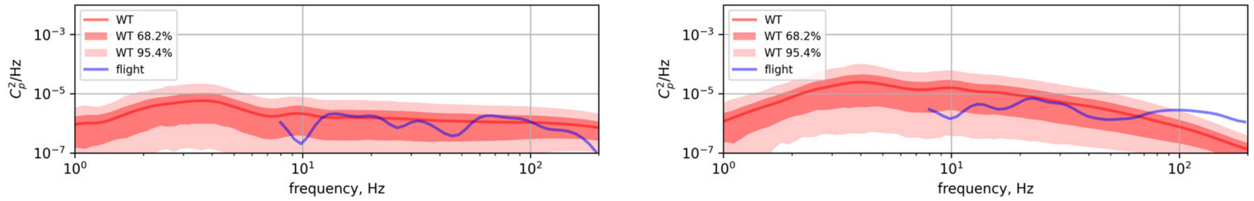

(e) Global CWTs, $M_\infty = 0.90$.

(j) Global CWTs, $M_\infty = 0.90$.

Station 13, flight PT located at $\theta = 95°$, WT matched PT located at $\theta = 90°$.

Station 16, flight PT located at $\theta = 181.8°$, WT matched PT located at $\theta = 180°$.

Fig. 29 Artemis I flight data compared to WT data from Test 645 for analysis stations on the LVSA and forward skirt.

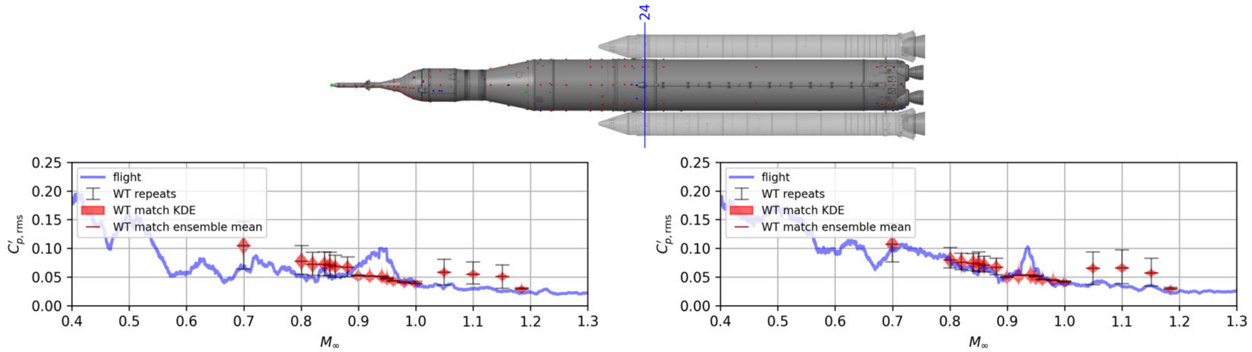

(a) $C'_{p,\mathrm{rms}}$.

(f) $C'_{p,\mathrm{rms}}$.

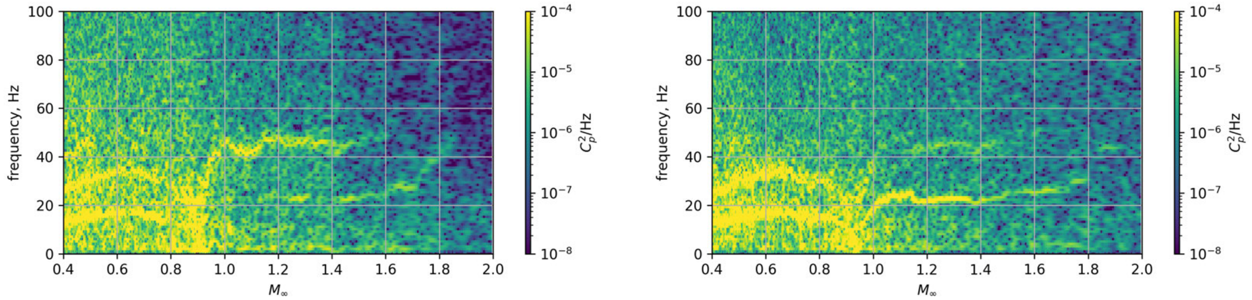

(b) C'_p spectrogram.

(g) C'_p spectrogram.

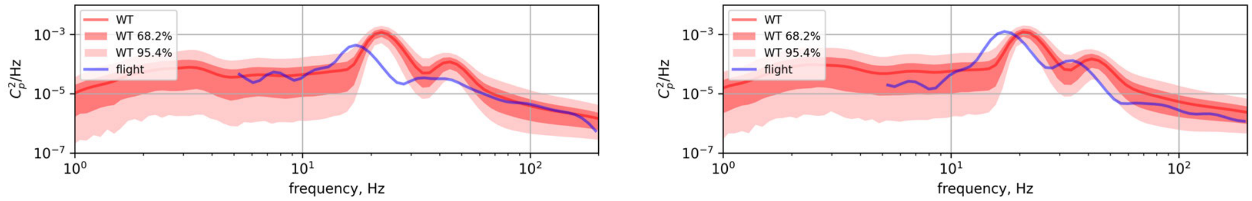

(c) Global CWTs, $M_\infty = 0.70$.

(h) Global CWTs, $M_\infty = 0.70$.

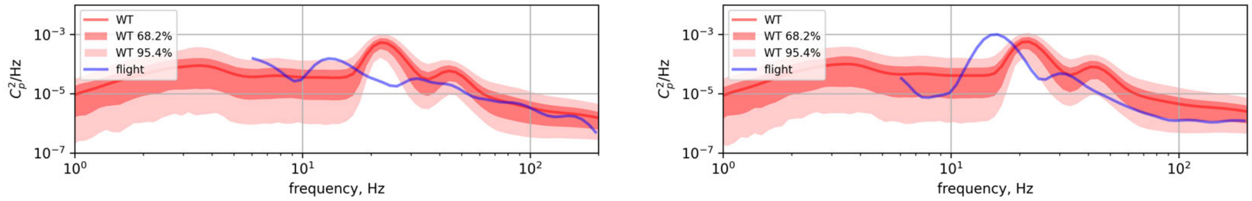

(d) Global CWTs, $M_\infty = 0.80$.

(i) Global CWTs, $M_\infty = 0.80$.

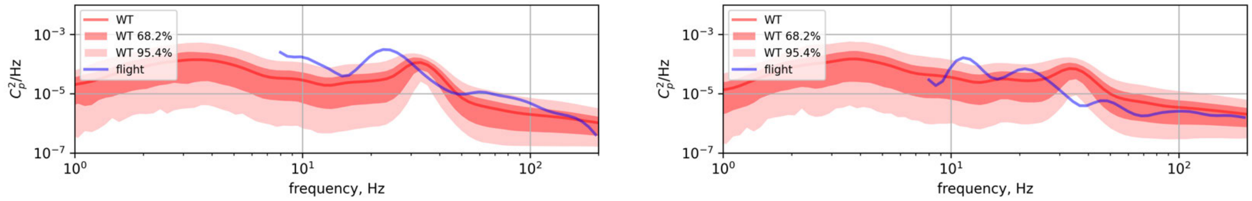

(e) Global CWTs, $M_\infty = 0.90$.

(j) Global CWTs, $M_\infty = 0.90$.

Station 24, flight PT located at $\theta = 88.65°$, WT matched PT located at $\theta = 90°$.

Station 24, flight PT located at $\theta = 268.70°$, WT matched PT located at $\theta = 270°$.

Fig. 30 Artemis I flight data compared to WT data from Test 645 for analysis station on the intertank downstream of the booster FAH.

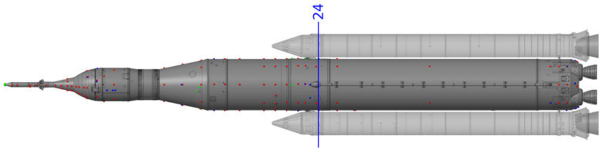

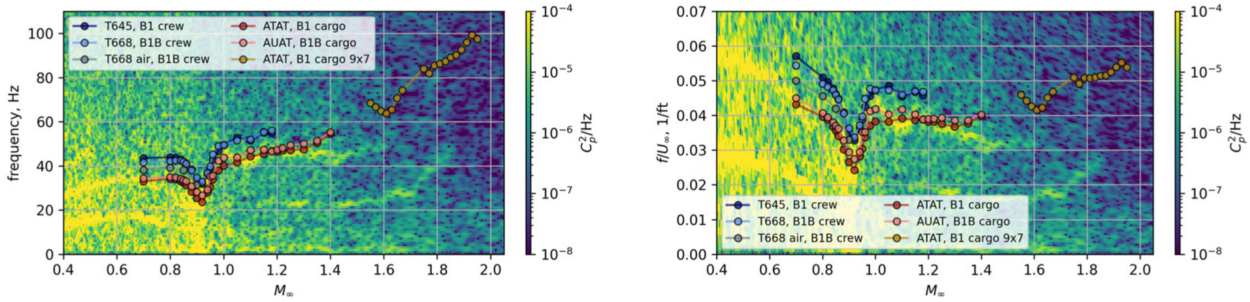

(a) Peak frequencies.

(b) Peak frequencies normalized by velocity.

(c) θ = 90°.

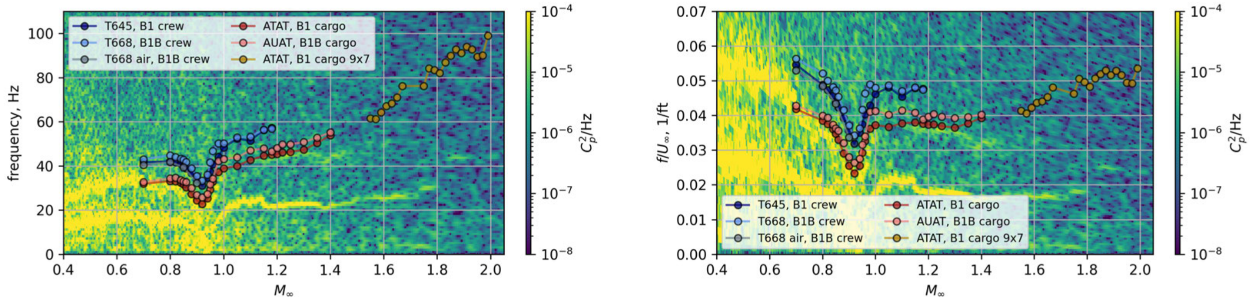

(d) Peak frequencies.

(e) Peak frequencies normalized by velocity.

(f) θ = 270°.

Fig. 31 Comparison of peak frequencies from WT tests versus M_∞ for PTs located at station 24, downstream of the FAH. WT data are overlaid on the flight data spectrogram for matched PT location.

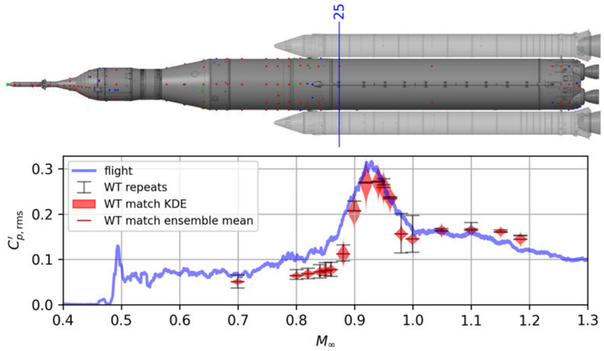

(a) $C'_{p,\text{rms}}$.

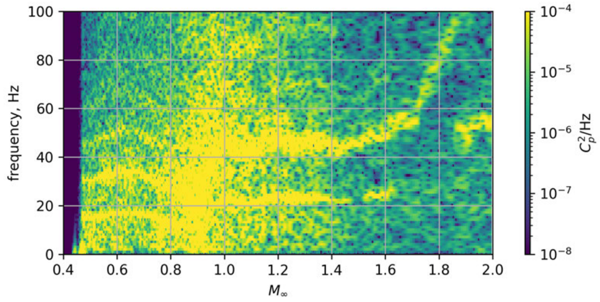

(b) C'_p **spectrogram.**

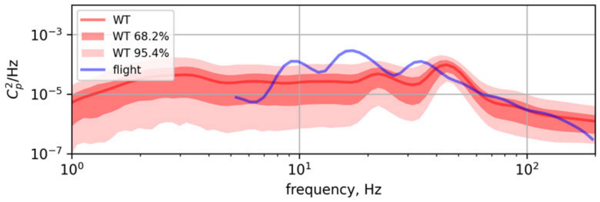

(c) Global CWTs, $M_\infty = 0.70$.

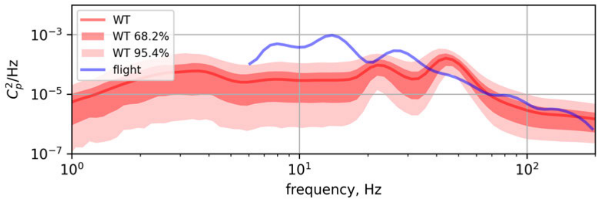

(d) Global CWTs, $M_\infty = 0.80$.

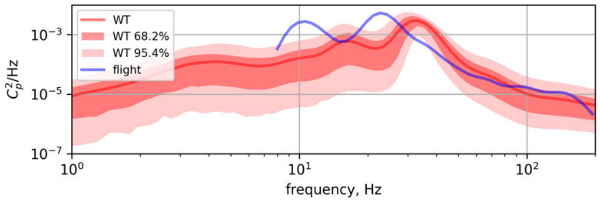

(e) Global CWTs, $M_\infty = 0.90$.

Station 25, flight PT located at $\theta = 90°$, WT matched PT located at $\theta = 90°$.

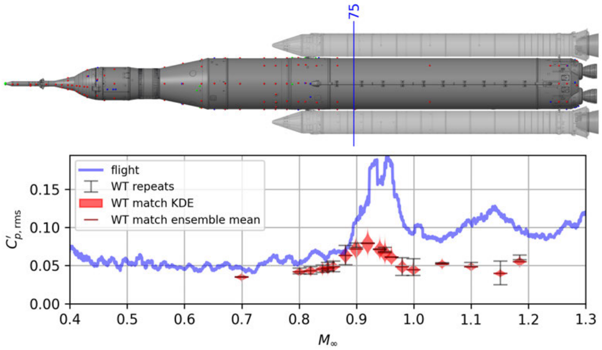

(f) $C'_{p,\text{rms}}$.

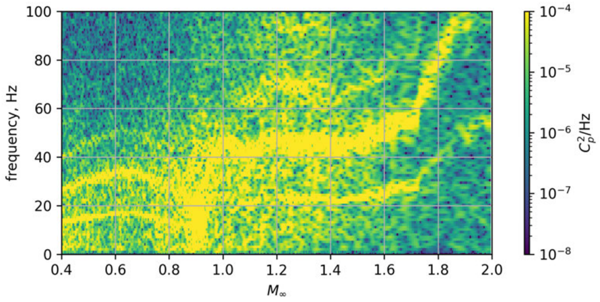

(g) C'_p **spectrogram.**

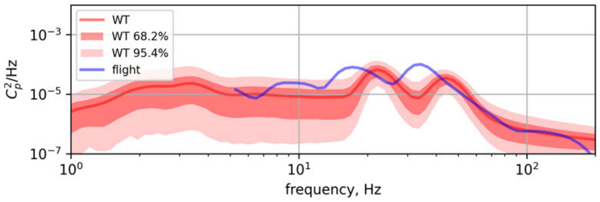

(h) Global CWTs, $M_\infty = 0.70$.

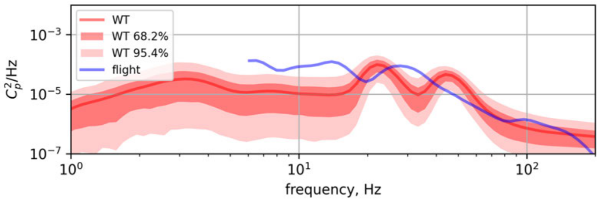

(i) Global CWTs, $M_\infty = 0.80$.

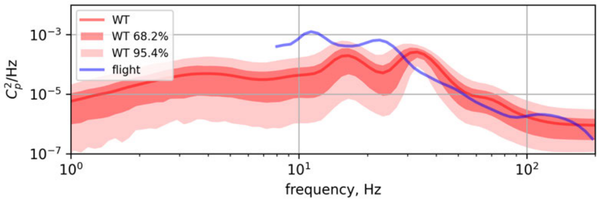

(j) Global CWTs, $M_\infty = 0.90$.

Station 75, flight PT located at $\theta = 87.78°$, WT matched PT located at $\theta = 90°$.

Fig. 32 Artemis I flight data compared to WT data from Test 645 for analysis stations on the LH2 tank downstream of the booster FAH.

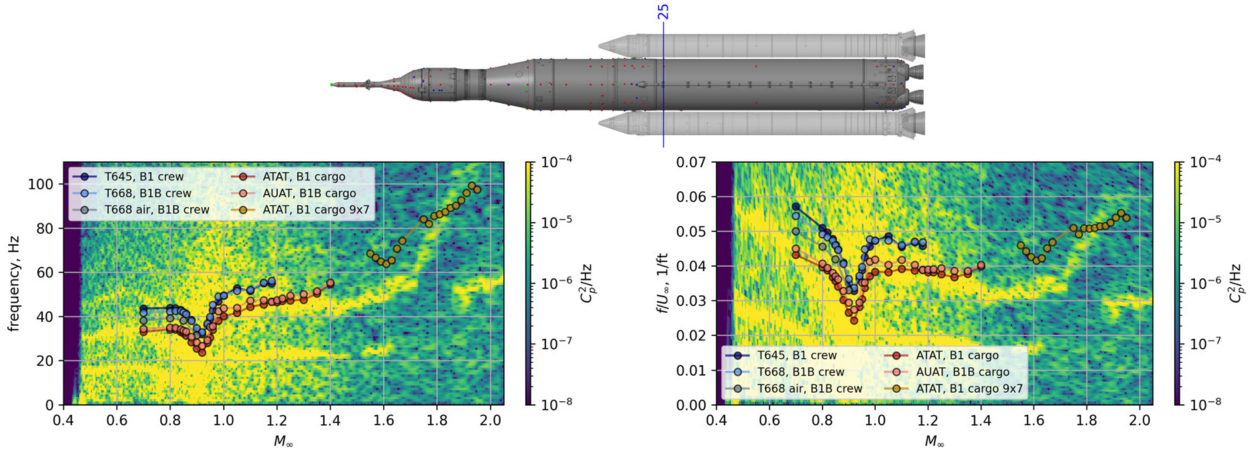

(a) Peak frequencies.

(b) Peak frequencies normalized by velocity.

(c) Station 25.

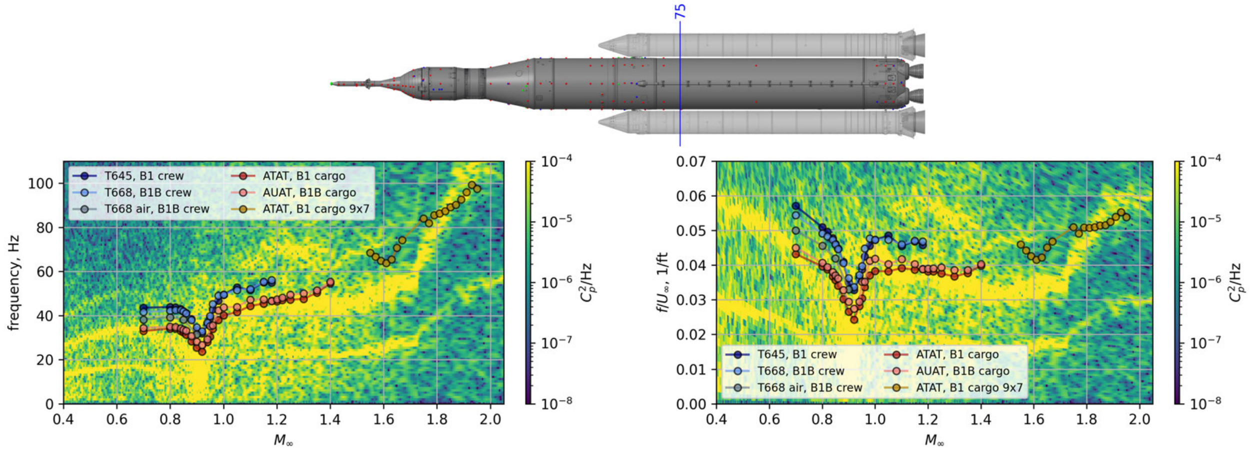

(d) Peak frequencies.

(e) Peak frequencies normalized by velocity.

(f) Station 75.

Fig. 33 Comparison of peak frequencies from WT tests versus M_∞ for PTs at $\theta = 90°$, facing the LSRB, downstream of the FAH. WT data are overlaid on the flight data spectrogram for matched PT location.

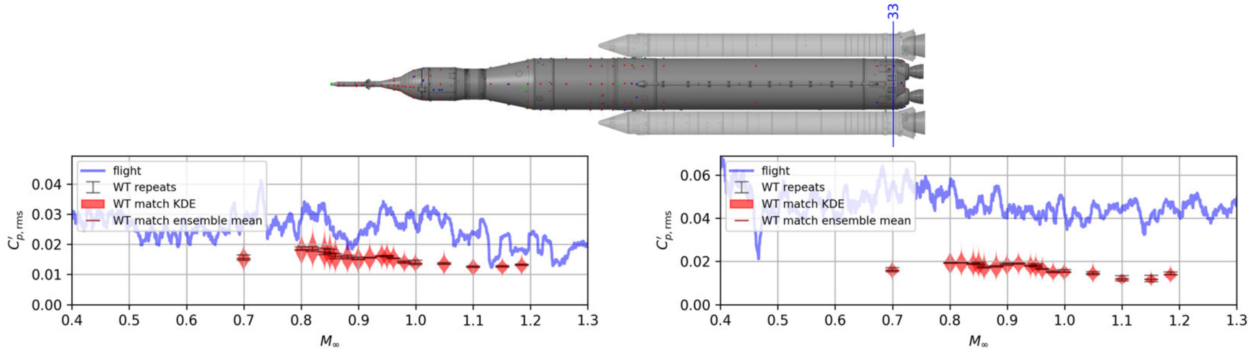

(a) $C'_{p,\text{rms}}$**.** **(f)** $C'_{p,\text{rms}}$**.**

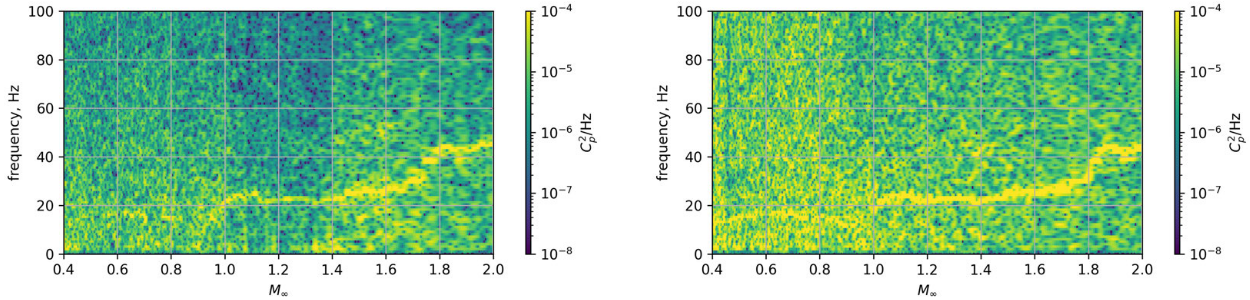

(b) C'_p **spectrogram.** **(g)** C'_p **spectrogram.**

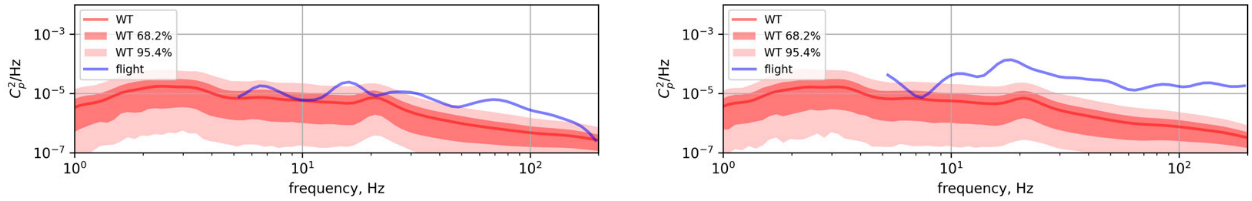

(c) Global CWTs, $M_\infty = 0.70$**.** **(h) Global CWTs,** $M_\infty = 0.70$**.**

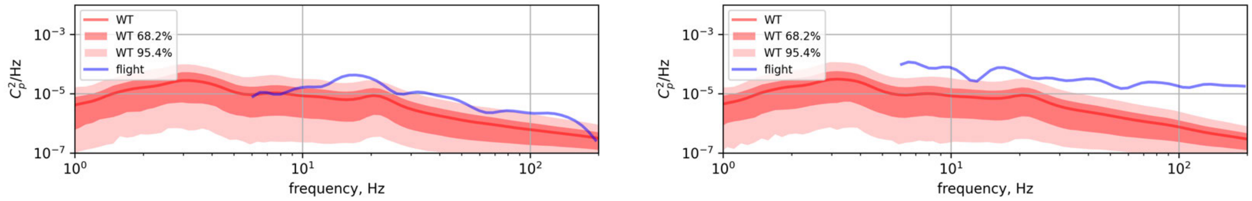

(d) Global CWTs, $M_\infty = 0.80$**.** **(i) Global CWTs,** $M_\infty = 0.80$**.**

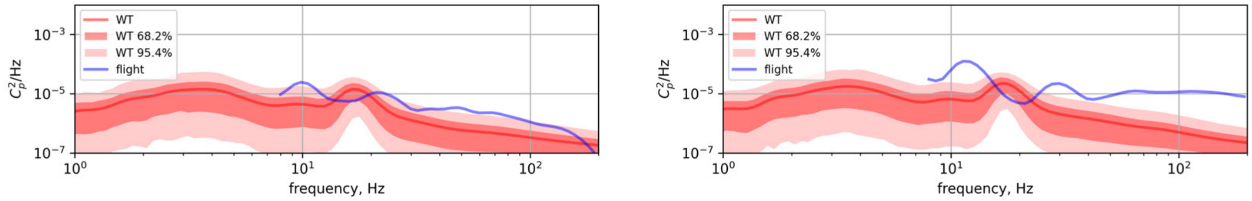

(e) Global CWTs, $M_\infty = 0.90$**.** **(j) Global CWTs,** $M_\infty = 0.90$**.**

Station 33, flight PT located at $\theta = 225°$**, WT matched PT located at** $\theta = 225°$**.**

Station 33, flight PT located at $\theta = 315.35°$**, WT matched PT located at** $\theta = 315°$**.**

Fig. 34 Artemis I flight data compared to WT data from Test 645 for analysis station on the engine section.

V. Conclusion

In this paper, repeat point data from the NASA LaRC TDT Test 645 at various M_∞ and $\alpha = \beta = 0°$ have been presented to give an overview of repeatability during SLS unsteady aerodynamics wind tunnel tests. In general, mean $C'_{p,\mathrm{rms}}$ compare well point-to-point, and the variation of $C'_{p,\mathrm{rms}}$ for flight-comparable windows within a single wind tunnel test point is consistent for that seen over all the repeats for a given sensor, vehicle attitude, and flight condition. This suggests that in comparing to flight data, using matched attitude and flight condition test points should yield good comparisons if the subscale test articles and methods are accurate representations of the full scale flight. Repeat point data from several other wind tunnel tests have also been presented to provide an overview for test-to-test and tunnel-to-tunnel repeatability. These results suggest that for matched sensors on the core stage at matched aerodynamic conditions and vehicle attitudes, the test-to-test variability in $C'_{p,\mathrm{rms}}$ is relatively low for tests conducted in the same facility, but can be significant for tests conducted at different facilities (NASA LaRC TDT versus the NASA ARC UPWT). Due to differences in the wind tunnel models tested, comparisons are only presented for sensors located on the core stage and mainly in the multibody region of the vehicle, where small geometric differences have been previously shown to lead to significant differences in the unsteady pressure field. The most significant difference discussed is the tunnel-to-tunnel variation in peak frequencies identified in the wake of the booster forward attachment hardware. The resulting unsteady pressure modes shed highly coherent vortices at distinct frequencies that are shown to consistently differ between tests conducted at the two facilities. Results comparing the tunnel test data with data acquired during the Artemis I flight test indicate that at the analysis stations discussed, $C'_{p,\mathrm{rms}}$ and C'_p spectra compare well for many stations on the vehicle. Significant differences in the multibody region of the vehicle, particularly in (1) the peak frequencies of the booster forward attachment hardware wake and (2) the spatial extent of high fluctuating environments associated with those unsteady pressure modes, are presented and discussed. Interestingly, the peak frequencies identified in the NASA ARC UPWT tests for these modes are closer to those measured during flight than the peaks identified using data acquired during the NASA LaRC TDT tests. Current computational studies and future experimental work are ongoing to better understand these differences between tunnels and between flight and tunnel.

References

[1] Rainey, A. G., "Progress on the Launch-Vehicle Buffeting Problem," *Journal of Spacecraft and Rockets*, Vol. 2, 1965, pp. 289–299. https://doi.org/10.2514/3.28174.

[2] Cole, H. A., Jr., Erickson, A. L., and Rainey, A. G., "Buffeting during atmospheric ascent," NASA SP-8001, Nov. 1970.

[3] Fleming, E. R., "Transonic Buffeting Loads Experience at The Aerospace Corporation," Tech. Rep. TOR-95(5530)-6, Mar. 1995.

[4] Kabe, A. M., "Time Domain Buffet Loads Analysis," Tech. Rep. TOR-2007(2209)-6078, Nov. 2006.

[5] NASA, "Load Analyses of Spacecraft and Payloads," NASA NASA-STD-5002A, 2019.

[6] Piatak, D. J., Sekula, M. K., and Rausch, R. D., "Test Summary Document for the SLS Rigid Buffet Model Test Program: TDT Test T632," NASA TM-2016-219218, 2016.

[7] Piatak, D. J., Sekula, M. K., and Rausch, R. D., "Test Summary Document for the SLS Rigid Buffet Model Test Program: TDT Test T645," NASA TM-2016-219332, 2016.

[8] Piatak, D. J., Sekula, M. K., Rausch, R. D., Florance, J. R., and Ivanco, T. G., "Overview of the Space Launch System Transonic Buffet Environment Test Program," *AIAA SciTech 2015*, 2015. https://doi.org/10.2514/6.2015-0557.

[9] Sekula, M. K., Piatak, D. J., Rausch, R., Florance, J. R., and Ramey, J., "Initial Assessment of Space Launch System Transonic Unsteady Pressure Environment," *AIAA SciTech 2015*, 2015. https://doi.org/10.2514/6.2015-0558.

[10] NASA, "Space Launch System Program Exploration Mission-1 (EM-1) Flight Evaluation Plan," NASA SLS-PLAN-100 Revision E, 2021.

[11] Heaney, P. S., Piatak, D. J., Sekula, M. K., and Soranna, F., "Comparison of Wind-Tunnel and Flight Unsteady Pressure Environments for the Ares I-X Flight Test Vehicle," *AIAA SciTech 2022*, San Diego, CA, 2022. https://doi.org/10.2514/6.2022-2413.

[12] Ericsson, L., and Reding, J., "Reynolds number criticality in dynamic tests," *16th Aerospace Sciences Meeting*, 1978. https://doi.org/10.2514/6.1978-166.

[13] Brauckmann, G. J., Streett, C., Kleb, W. L., Alter, S. J., Murphy, K. J., and Glass, C., "Computational and Experimental Unsteady Pressures for Alternate SLS Booster Nose Shapes," *AIAA SciTech 2015*, 2015. https://doi.org/10.2514/6.2015-0559.

[14] Ramey, J. M., Giles, I. M., Goushcha, O., Heaney, P. S., Piatak, D. J., Sekula, M. K., and Soranna, F., "Parametric Study of the Forward Attachment Geometry for the Space Launch System Next Generation Booster," *AIAA SciTech 2023*, National Harbor, MD, 2023. https://doi.org/10.2514/6.2023-0427.